



UVLM-based mesh generator intended for onshore and offshore wind farms

Bruno A. Roccia¹, Luis R. Ceballos², Marcos L. Verstraete², and Cristian G. Gebhardt¹

¹Geophysical Institute and Bergen Offshore Wind Centre (BOW), University of Bergen, Norway

²Group of Applied Mathematics, Universidad Nacional de Río Cuarto, Argentina

Correspondence: Bruno A. Roccia (bruno.roccia@uib.no)

Abstract. In the last decades, the unsteady vortex-lattice method (UVLM) has gained a lot of acceptance to study large onshore/offshore wind turbines (WTs). Furthermore, and due to the development of more powerful computers, parallelization strategies and algorithms like the fast multipole method, it is possible to use vortex-based methods to analyze and simulate wind farms (WFs). However, UVLM-based solvers require structured meshes, which are generally very tedious to build using classical mesh generators, such as those utilized in the context of finite element methods (FEMs). Wind farm meshing is further complicated by the large number of design parameters associated with the wind turbine (pre-cone angle, tilt angle, blade shape, etc.), farm layout, modeling of the terrain topography (for onshore WFs), and modeling of the sea level surface (for offshore WFs), which makes the use of FEM-oriented meshing tools almost inapplicable.

In the literature there is a total absence of meshing tools when it comes to building aerodynamic grids of WTs and WFs to be used along with UVLM-based solvers. Therefore, in this work, we present a detailed description of the geometric modeling and computational implementation of an interactive UVLM-oriented mesh generator, named *UVLMeshGen*, developed entirely in Matlab[®] and easily adaptable to GNU OCTAVE, for wind turbines and onshore/offshore wind farms. The meshing tool developed here consists of: *i*) a geometric processor in charge of designing and discretizing an entire wind farm; and *ii*) an independent module in charge of computing the kinematics for the entire WF. The output data provided by the *UVLMeshGen* consist of nodal coordinates and connectivity arrays, making it especially attractive and useful to be used by other flow potential solvers using: doublets, sources and sinks, or dipoles, among others. The work is completed by providing a series of aerodynamic results related to WTs and WFs to show the capabilities of the mesh generator, without going into detailed discussions of wind turbine aerodynamics, which are not the focus of this paper. The meshing tool developed here is freely available under a Creative Commons Attribution 4.0 International License Roccia (2023).

1 Introduction

For some years now, wind energy has become one of the fundamental pillars on the world stage of renewable energy. This fact has been materialized by an increasing number of different wind turbine (WT) designs: going from small wind turbines (e.g., the Vestas V27 of 200 KW Torabi (2022)) and moderately sized designs for onshore applications to the incredibly large



offshore WTs such as the Vestas V236-15.0MW prototype Vestas (2022) or the CSSC Haizhuang H260-18MW concept design
25 with a rotor diameter of 260 m CSSC Haizhuang (2023).

One of the most important challenges of this technology is the accurate characterization of the WT loads under inflow
conditions which may trigger complex aerodynamic effects. Although the description of the flow surrounding a wind turbine
has been a subject of interest for many years, the study of three-dimensional and expensive-to-model unsteady aerodynamics
of WTs and wind farms is still an active field of research Muñoz-Simón et al. (2022). Throughout the years, a wide variety
30 of aerodynamic models for wind turbines have been proposed, verified, validated, and successfully implemented and applied.
They range from basic approaches such as those based on the *blade element momentum* (BEM) theory, widely spread through
the industry for the initial design loops, to advanced high-fidelity models using, for example, *computational fluid dynamics*
(CFD) techniques.

Despite classical and enhanced versions of BEM-based solvers have been found to provide good agreement with mea-
35 surements and CFD simulations, they require a series of engineering corrections to model challenging unsteady aerodynamic
phenomena of increasingly large WTs Perez-Becker et al. (2020). The fluctuations or overestimations observed in BEM simula-
tions, when compared to more sophisticated approaches, are a natural consequence of the underlying theory behind the method
Hansen (2008). Instead, high-fidelity CFD computations can capture more flow physics, thus providing a better prediction
accuracy than BEM codes Nigam et al. (2017); Liu et al. (2017). However, solving the full Navier–Stokes equations for three-
40 dimensional unsteady flows with boundaries undergoing large and complex motion is by far a challenging and time-consuming
task (requiring typically from two to five weeks in average) Terry (2018).

As a third option, we can introduce the so-called vortex-lattice methods (VLMs), which represent an excellent alternative to
assess the aerodynamic performance of different aeronautical/mechanical engineering applications. Its extension to the study of
transient aerodynamic loads for slender lifting surfaces undergoing complex motions, the well-known unsteady vortex-lattice
45 method (UVLM), has already proven to be a more than viable option presenting an excellent trade-off between precision and
computational cost Verstraete et al. (2023). Furthermore, UVLM-based solvers have been continuously gaining ground in the
context of those problems, in which free-wake methods become a necessity due to the geometric complexity and the presence
of large displacement/rotations, such as: morphing wings Verstraete et al. (2015, 2019), flapping wings Stanford and Beran
(2010); Rocca et al. (2013); Nguyen et al. (2016), rotorcraft Wie et al. (2009); Colmenares et al. (2015); Lee et al. (2022),
50 wind turbines Garrel (2003); Gebhardt et al. (2010); Gebhardt and Rocca (2014), and non-conventional wind energy devices
Abdelkefi et al. (2014); Beltramo et al. (2020); Rocca et al. (2020), among others.

Among the most promising UVLM-based solvers capable of performing aerodynamic analysis of wind turbines, we can
mention OpenVOGEL Hazebrouck (Accessed June 14, 2023), WinDS WinDS (Accessed June 14, 2023), GSF-Aero Verstraete
et al. (2023), the general-purpose framework developed by Perez Segura et al. Pérez Segura et al. (2020), and VLMSim
55 Verstraete et al. (2023). Where the latter one can handle aerodynamic studies of arbitrary onshore and offshore wind farms.
Although UVLM frameworks are mid-fidelity simulation tools with an enormous potential to be used in the wind energy sector,
they require structured meshes enriched with specific data, which are very tedious to build by using classical meshing codes



as those utilized in the context of the finite element method (FEM), such as: Gmsh, CUBIT[®], MeshLab, and GID[®], among others.

60 In addition, wind turbines are characterized by a large number of design parameters, such as: the pre-cone angle, the tilt angle, multiple airfoils defining the blade, the twist angle, pre-bend and pre-sweep shapes, etc. In this sense, a proper wind turbine meshing process should incorporate an easy way to handle such information. When considering wind farms, the meshing is further complicated by the need of including parameters associated with the farm layout, terrain topography (for onshore wind farms), and the description of the sea level surface for offshore wind farms. Another key point, and by no means less important, 65 is the generation of the kinematics for the entire wind farm. This aspect includes everything from basic rotor kinematics and laws of motion for yaw and pitch (if any) to sea level surface kinematics (to simulate waves) and substructure motions for floating wind turbines Sant and Cuschieri (2016); Lee and Lee (2019). On this basis, a versatile UVLM-oriented meshing tool for onshore and offshore wind farms must necessarily involve *design* plus *discretization* plus *kinematic* modules to provide all the data required by any standard UVLM engine chosen.

70 To the best of our knowledge, there is to date no freely-available UVLM-oriented mesh generator intended for arbitrary wind farms that allows for: *i*) designing wind park layouts; *ii*) considering different wind turbines (with their own design parameters); *iii*) including the terrain topography and/or the sea surface description; and *iv*) computing the wind farm kinematics. The only attempts of which we are aware of are those individual efforts to mesh specific geometries and power-limited meshing tools already incorporated into UVLM codes such as OpenVOGEL or in-house modules developed at companies that are not of open 75 access for the wind energy community.

In this work, we present a detailed description of the geometric modeling and computational implementation of an interactive UVLM-oriented mesh generator for onshore and offshore wind farms, hereinafter referred as UVLMeshGen. The meshing tool, fully developed in Matlab[®] language and easily adaptable to GNU OCTAVE, allows for the generation of structured and conformal aerodynamic grids of wind farms, including the terrain and/or sea level surface modeling. The output data provided 80 by UVLMeshGen consists of nodal coordinates and connectivity arrays, similar in some way to classical FEM-oriented mesh generators. In this regard, such output data are not limited to only UVLM-based simulation frameworks, but they can be used by any flow potential solver relying on other singularities elements, such as: doublets, sources and sinks, or dipoles, among others. Besides the geometric processor, UVLMeshGen has an additional independent module in charge of computing, according to user-defined input data, the kinematics for the entire wind farm. Furthermore, this meshing engine allows the addition of 85 user-defined scripts or add-ons to post-process the aerodynamic grids and/or to enrich their data structure with additional information in order to be used as input data in any kind of UVLM solver. All these features make the meshing tool presented here a valuable resource to be used in larger projects and endeavors such as AVATAR (Advanced Aerodynamic Tools for Large Rotors, 2013-2017), which pursued, as main goal, the assessment of different aerodynamic models for large (10MW+) wind turbines Schepers (2015) or the CRC 1463 Offshore Megastructures (Integrated design and operation methodology for offshore megastructures, 2021-2024) targeting an integrative design and operation for offshore wind turbines (20MW+) Hannover 90 (2021). UVLMeshGen is freely available under a Creative Commons Attribution 4.0 International License Rocca (2023).



The remainder of this work is organized as follows: In Section 2, we introduce the geometric entities used and the meshing process followed to obtain the aerodynamic grid of each component of a wind turbine. In Section 3, we describe the main aspects associated with the computational implementation of the UVLMeshGen. In Section 4, we briefly describe the aerodynamic model behind classical UVLM implementations, including the wakes' free convection, the computation of unsteady loads and its discretization in space and time. In Section 5, we present a series of aerodynamic simulations to show the capabilities of the mesh generator, without entering into quantitative discussion about aerodynamic of wind turbines. Finally in Section 6, we provide conclusions and future work to be addressed in a sequel.

2 Geometric Modelling

It is well-known that a wind turbine is characterized by a large number of parameters. A proper aerodynamic analysis of such mechanical systems by UVLM-based codes necessarily requires an accurate description of the wind turbine surfaces. On this basis, this section first presents the geometric object to be used to represent the surfaces of a wind turbine. This subsection is followed by a full description of the geometric modeling of each component of a wind turbine (e.g., Hub, nacelle, blades, tower, etc.).

2.1 Geometric preliminaries

In case of using boundary element methods (BEMs) to predict the aerodynamic forces and wake structures of very complex engineering systems, an accurate description of their boundaries (solid surfaces) is mandatory. In particular, the aerodynamic analysis of wind turbine farms by using BEMs requires to provide: *i*) precise data associated with the discretization of their boundaries (ground, rotors, towers, etc); *ii*) additional data according to the method adopted (collocation points, shedding zones, type of singularities, etc); and *iii*) kinematics of the system (positions and velocities over time).

In general, the main components of a wind turbine are: the hub, the nacelle, the blades, the tower, and the ground where the turbine is located. For offshore WTs, we need to add the substructure, which can be fixed or floating depending on whether the WT is placed in shallow, moderately deep, or deep waters. On this basis, two different geometric entities can be identified as the basic ones from which all the discretized surfaces of a WT farm will be built. These are: a hole plate (called GO_1), and a skinned surface (called GO_2), see Fig. 1. Although entities GO_1 and GO_2 are equivalent from a topological point of view, they are obtained by following different geometric construction procedures. In view of this, and according to the geometric modeling spirit of the current work, it is necessary to make a distinction between them.

Here, both objects, GO_1 and GO_2 , are build from the very beginning as discretized surfaces by using quadrilateral elements QE (also called cells, panels or boundary elements). Such simple geometrical elements were chosen because most of VLM- or PM-based codes rely on QE discretizations to represent the lifting and non-lifting surfaces. Next, we present a detailed description of how these objects are build through a discretized setting by using QE .

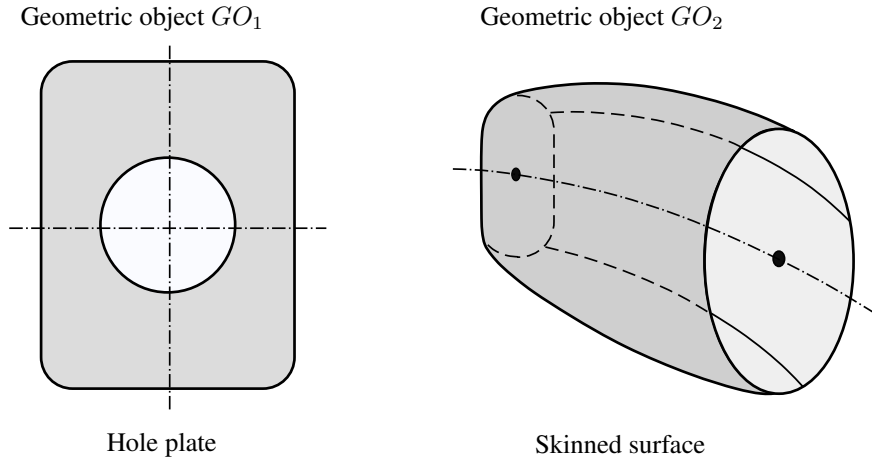


Figure 1. Basic geometric entities.

2.1.1 Object GO_1

This kind of object consists of a rectangular plate together with a circular or ellipsoidal hole. In order to mesh it with QE we make use of the *FG-squirircular mapping*¹, which allows to smoothly transform a circular domain $\mathcal{D} = \{(u, v) \in \mathbb{R}^2 \mid u^2 + v^2 \leq r^2\}$ into a square region $[-r, r] \times [-r, r]$ parameterized as $\mathcal{S} = \{(x, y) \in \mathbb{R}^2 \mid x^2 + y^2 - x^2y^2 \leq r^2\}$ Fernandez-Guasti (1992). Knowing that \mathcal{D} and \mathcal{S} can be represented as a set of concentric circles and shrunken FG-squircles, we can establish a correspondence between the r -disc and the $2r$ -square region by mapping every circular contour in the interior of the disc to a squirircular contour in the interior of the square (see Fig. 2).

According to Fong Fong (2021), an intermediate shape between a circle and a square can be represented by the following implicit equation,

$$x^2 + y^2 - \frac{s^2}{r^2}x^2y^2 = r^2, \quad (1)$$

where (x, y) is a set of Cartesian coordinates in \mathbb{R}^2 , s is the so-called squareness parameter which allows the shape to be interpolated between a circle and a square, and r is the radius of the original circle. While $s = 0$ generates a circle of radius r , $s = 1$ produces a square with a side length of $2r$. In turn, (1) can be slightly modified to allow an ellipse to be smoothly transformed into a rectangle. Such a representation is given as follows,

$$\frac{x^2}{r_x^2} + \frac{y^2}{r_y^2} - \frac{s^2}{r_x^2 r_y^2} x^2 y^2 = 1. \quad (2)$$

¹In this work we use the term *squiracle* to make reference to an intermediate shape between a circle and a square, first introduced by Fernandez Guasti Fernandez-Guasti (1992). Then, the Fernandez Guasti squiracle shape is denoted as *FG-squiracle* for short.

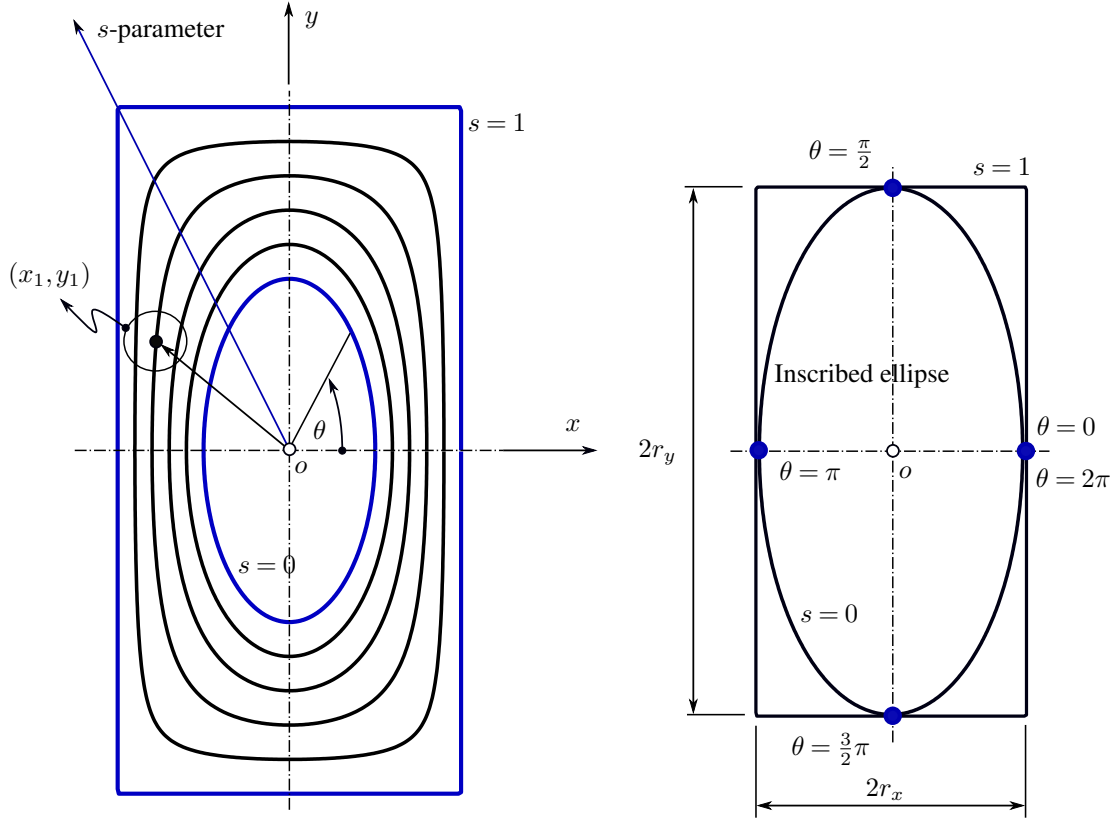


Figure 2. Geometric object GO_1 - squircle shapes.

When $s = 0$, we obtain the equation of an ellipse with semi-axes r_x, r_y ; when $s = 1$ we obtain the equation for a rectangle with sides $2r_x, 2r_y$. In order to facilitate the computation of intermediate shapes, (2) is recast in parametric form through the mapping $\Phi(\theta) : \mathbb{R}_\theta \rightarrow (x, y) \in \mathbb{R}^2$ as,

$$140 \quad \Phi(\theta) = \begin{cases} x(\theta) \\ y(\theta) \end{cases} = \begin{cases} \frac{r_x \text{Sgn}(\cos \theta)}{s\sqrt{2}|\sin \theta|} \sqrt{1 - \sqrt{1 - s^2 \sin^2 2\theta}} \\ \frac{r_y \text{Sgn}(\sin \theta)}{s\sqrt{2}|\cos \theta|} \sqrt{1 - \sqrt{1 - s^2 \sin^2 2\theta}} \end{cases}, \quad (3)$$

with $\theta \in \mathbb{R}_\theta = \{\theta \mid 0 \leq \theta \leq 2\pi\} \setminus F_\theta$, $F_\theta = \{0, \frac{\pi}{2}, \pi, \frac{3}{2}\pi, 2\pi\}$, and provided that $s \neq 0$. On one hand, when $s = 0$ the shape corresponds to a circle/ellipse and therefore (3) reduces to the well-known parametric equation of a circle/ellipse. On the other hand, for $\theta \in F_\theta$, (3) becomes indeterminate and an alternative expression must be used. A deeper look at the FG-Squircular mapping allows us to recognize that, for given r_x and r_y , the values of $\theta \in F_\theta$ generate points on both contours, the rectangle and its inscribed ellipse (see Fig. 2). Therefore, we can again use the parametric equations of the ellipse to map F_θ .

145

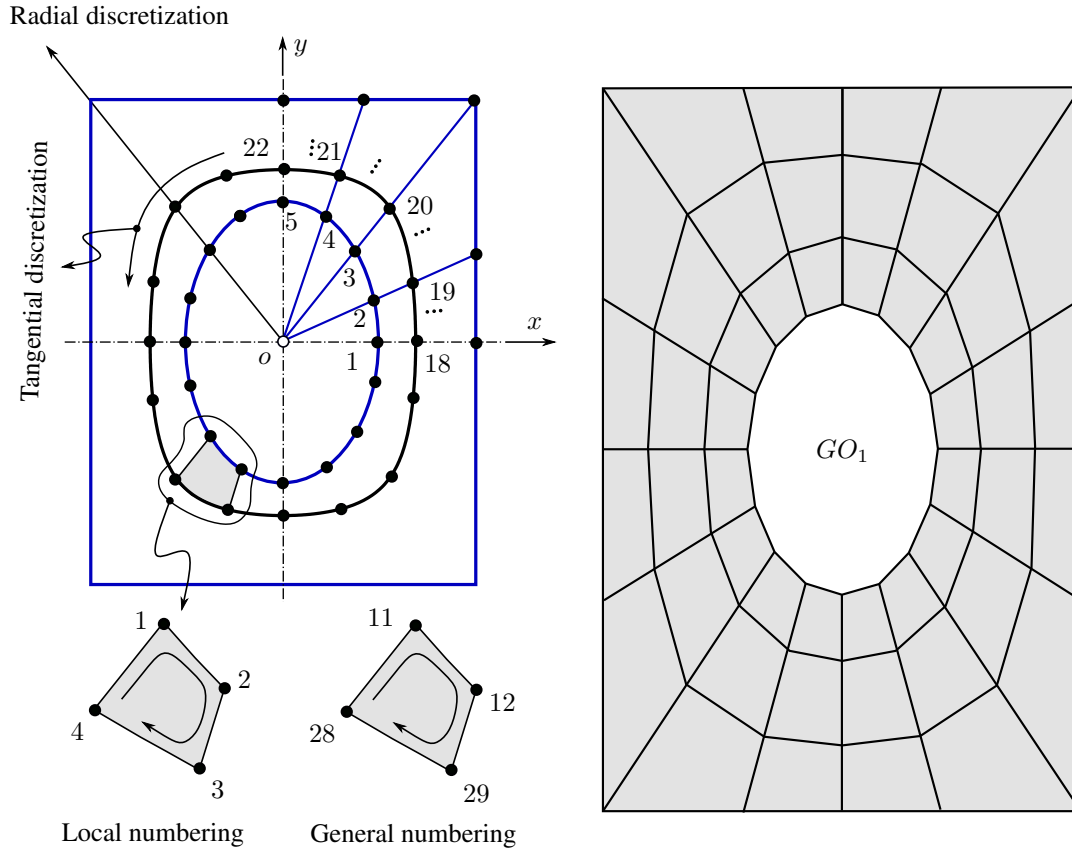


Figure 3. GO_1 - (left) discretization procedure, (right) typical mesh.

The object GO_1 is geometrically decomposed into a finite set of quadrilateral cells $\mathcal{A}_{GO_1} = \{B_k\}$ as,

$$\mathcal{A}_{GO_1} = \bigcup_{k \in E_1} B_k,$$

where $E_1 = \{1, 2, \dots, (N_r - 1)(N_c - 1)\}$, N_r is the number of intermediate shapes (including both inner and outer contours), and N_c is the number of elements along their tangential direction. The total number of cells (or panels) is then given by the cardinal of E_1 , i.e., $\text{card}(E_1)$. In Fig. 3 (left) we present a schematic of how the division along the radial and tangential directions are performed. In Fig. 3 (right) we show the final mesh of a typical GO_1 for $N_r = 4$ and $N_c = 17$ thus giving $\text{card}(E_1) = 48$ panels.

2.1.2 Object GO_2

Surface generation in the context of computer-aided design (CAD) is typically done by using *lofting* or *skinning* processes. Although surface skinning is considered, according to Ball Ball (1993), as a kind of lofting, some differences have been



introduced throughout the years. However, both processes are intended for passing a surface through a set of so-called cross-sectional curves. In this work, we adopted a specific skinning procedure, hereafter referred as *ruled skinning*.

Ruled skinning provides the ability to skin a series of three or more profiles by placing ruled surfaces in between each section of profiles (see Fig. 4a). In turn, a ruled surface is defined by the property that through every point in the surface, there is at least one straight line which also lies in the surface. We can define a ruled surface more formally as a two-dimensional differentiable manifold constructed as the union of one parametric family of lines.

Definition 2.1 (Ruled surface). The following three definitions of a ruled surface are equivalent Biran (2019):

1. A surface such that through each point of it passes a straight line that is fully contained in the surface.
2. A surface generated by the motion of a straight line.
3. The set of a family of straight lines depending on a parameter that spans a set of real numbers.

Mathematically, a ruled surface can be described by,

$$\begin{aligned}
 \mathbf{R}(u, v) &= \mathbf{C}_1(u) + v \mathbf{r}(u), \quad v \in \mathbb{R} \\
 &= (1 - v) \mathbf{C}_1(u) + v \mathbf{C}_2(u),
 \end{aligned} \tag{4}$$

where $\mathbf{C}_k : \mathbb{R} \rightarrow \mathbb{R}^3$ is a parameterization for the curve $C_k \subset \mathbb{R}^3$. Any curve $\mathbf{R}(u_0, v)$ with fixed parameter u_0 is a *generator* line, the curve C_k is a *directrix* of the representation, and the vectors $\mathbf{r}(u) \neq \mathbf{0}$ describe the directions of the generators. Alternatively, we can generate a ruled surface by starting with two non-intersecting curves $\mathbf{C}_1(u)$ and $\mathbf{C}_2(u)$ as directrices and get the line directions as $\mathbf{r}(u) = \mathbf{C}_2(u) - \mathbf{C}_1(u)$ (see Fig. 4b).

In the context of wind turbines, some components (hub, nacelle, blades), although easily generated by a skinning process for modeling purposes, they cannot be represented by ruled surfaces. As an example, let us consider the surface \mathcal{R} shown in Fig. (4c). It is not a ruled surface if considered as a whole (first definition in 2.1). However, \mathcal{R} can be obtained as the union of three ruled surfaces. Furthermore, every GO_2 -object is geometrically decomposed into a finite set of quadrilateral cells $\mathcal{A}_{GO_2} = \{B_k\}$ as follows,

$$\mathcal{A}_{GO_2} = \bigcup_{i \in R_S} \mathcal{A}_{GO_2}^i, \quad \text{and} \quad \mathcal{A}_{GO_2}^i = \bigcup_{k \in E_{2,1}} B_k, \tag{5}$$

where $R_S = \{1, 2, \dots, N_{rs}\}$, N_{rs} is the number of ruled surfaces in what \mathcal{A}_{GO_2} is decomposed, and $E_{2,i}$ is a finite subset of \mathbb{N} . Then, the total number of QE used to discretize \mathcal{A}_{GO_2} is calculated as $\sum_{i=1}^{N_{rs}} \text{card}(E_{2,i})$. In Fig. (4d) we present the mesh of a typical hub nose, represented by $N_{rs} = 9$ and $\text{card}(E_{2,i}) = 24$, thus giving a total of 216 panels.

Finally, it should be stressed that any pair of cells belonging to GO_1 or GO_2 must meet the following requirements:

- If $B_k \cap B_j$ for $k \neq j$ is exactly one point, then it is a common vertex (node) of B_k and B_j .
- If $B_k \cap B_j$ for $k \neq j$ is not exactly one point, then it is a common facet of B_k and B_j (edge in two dimensions).

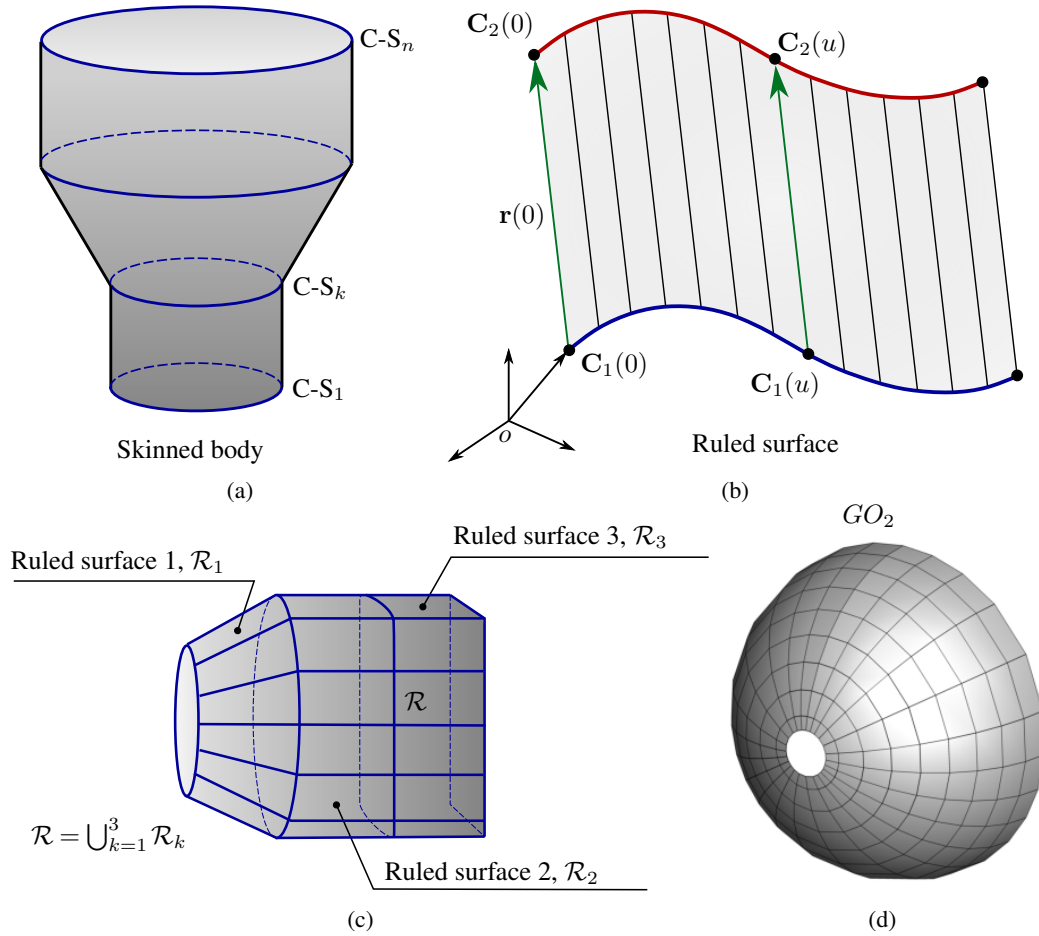


Figure 4. (a) Skinned body ($C-S_k$ stands for cross-section k), (b) Ruled surface, (c) Representation of a skinned body as a set of ruled surfaces, (d) typical mesh of a GO_2 .

2.2 Wind turbine farm modeling

185 Here, we present a detailed description on how the surface of each component in a wind turbine farm is modeled in terms of the
 geometric objects already introduced in Subsection 2.1. Fig. 5 provides a summary on which type of geometric object (GO_1
 or GO_2) are involved in generating the discretized surface associated with each component of a wind turbine. From now on,
aerodynamic mesh, or *bound vortex-lattice*, will be used interchangeably to make reference to a discretized surface.

Each wind turbine can be composed, at most, of six different components, namely:

- 190
- **Blade:** they are responsible for capturing part of the energy available in the wind.
 - **Hub:** it supports the blades and houses the pitch system.
 - **Nacelle:** it houses the components that convert mechanical energy into electrical energy.

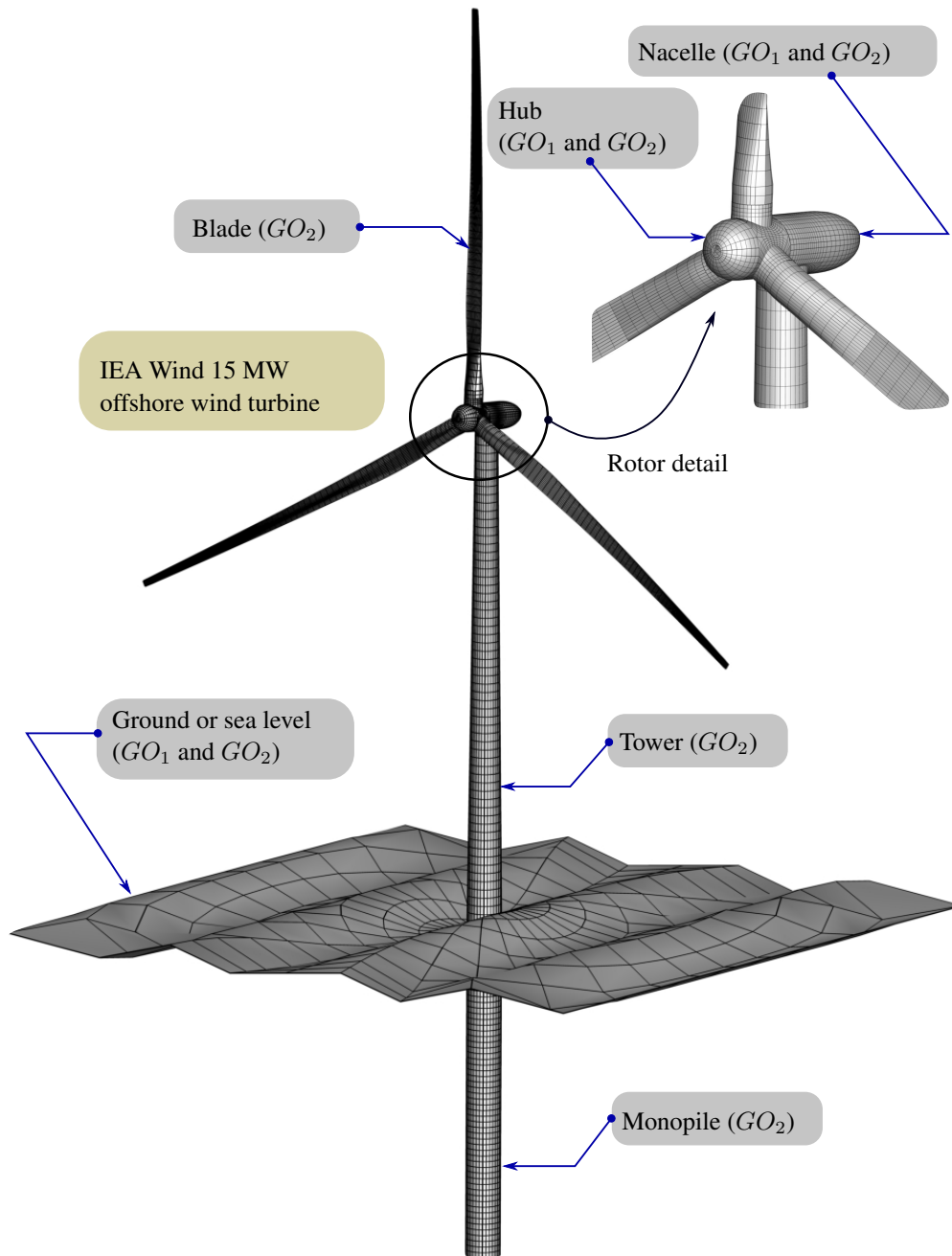


Figure 5. Geometric modeling of a wind turbine: IEA Wind 15 MW Offshore Reference Wind Turbine.

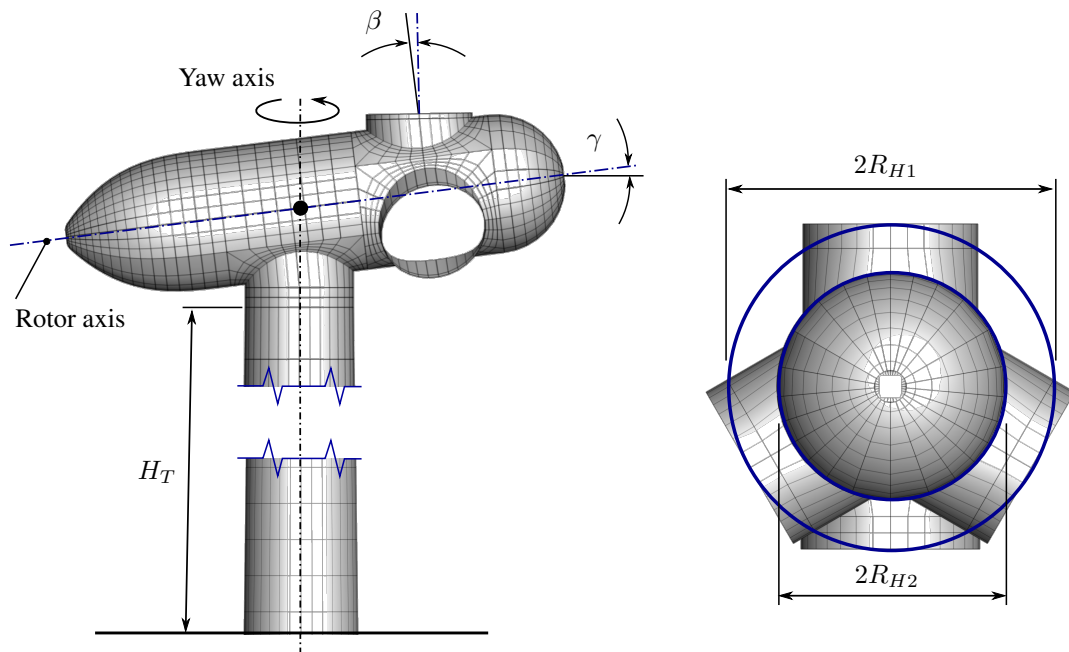
- **Tower:** it gives height to the rotor and supports the mass of the nacelle, hub, and blades.
- **Ground:** it represents either the terrain for onshore wind turbines or the sea surface for offshore wind turbines.



195 – **Monopile:** it holds the tower and the rest of wind turbine components above the sea floor.

Table 1. Standard parameters of a wind turbine

Variable	Structure field name	Description
N_B	NumBld	Number of blades
β	PreCone	Rotor precone angle [°]
γ	Tilt	Tilt angle [°]
R_{H1}	HubRad	Hub radius (including hub-to-blade connectors)
R_{H2}	HubInnerR	Hub radius (without hub-to-blade connectors)
H_T	TowHeight	Tower height



The user can generate different wind turbine configurations by turning any of these components on or off. In the following subsections we will discuss in detail how to model each component and what parameters should be provided to generate them. All these parameters are specified through some options available in the main mesher script, as well as through a configuration ASCII file. This topic will be covered to some extent in Section 3 on computational implementation.

200 As usual, some of those parameters are related to the global configuration of the wind turbine; these are listed in Table 1. To complete the turbine setup, it is also required to indicate which components should be considered to build the wind turbine mesh (see Table 2).



Clearly, the number of blades cannot be increased indiscriminately. If this happens, there may be geometric interference between the hub surface and blade roots. Furthermore, as the number of blades is becoming larger and larger, it may happen that two blades are very close to each other and therefore some geometrical interference may arise between them.

Table 2. Wind turbine components

Variable	Structure field name	Description
*	Blade	Blade geometry (0: OFF / 1: ON)
*	Tower	Tower geometry (0: OFF / 1: ON)
*	Nacelle	Nacelle geometry (0: OFF / 1: ON)
*	Hub	Hub geometry (0: OFF / 1: ON)
*	Ground	Ground geometry (0: OFF / 1: ON)
*	Monopile	Monopile geometry (0: OFF / 1: ON)

2.2.1 The tower and monopile

Such two components are essentially of the same kind. Both of them are ruled surfaces and therefore generated by GO_2 -like entities. As input data necessary to generate the aerodynamic mesh associated with the tower and monopile we need to provide: the diameter at the ends of the component, its length, and number of aerodynamic nodes along its longitudinal and tangential directions. Tables A.1 and A.2 in Appendix A provide a summary of the variables associated with both components.

2.2.2 The nacelle

The aerodynamic mesh of the nacelle \mathcal{N} is generated as the union of four sub-meshes, namely: *i*) the tower-nacelle connector $\mathcal{N}_{GO_2}^1$, *ii*) a curved patch $\mathcal{N}_{GO_1}^2$, *iii*) a cylindrical surface $\mathcal{N}_{GO_2}^3$, and *iv*) the tail of the nacelle $\mathcal{N}_{GO_2}^4$. All nacelle components are generated by GO_2 -like entities with the exception of the curved patch, which is of type GO_1 . Fig. 6 shows an exploded schematic of a typical nacelle of a wind turbine.

Among the several parameters involved in the design of wind turbines, the cone angle, tilt angle, and pitch angle are directly related with the aerodynamic behavior of the rotor. In particular, the tilt angle is used to provide sufficient clearance between the rotor blades and the tower. Here, for meshing purposes, such tilt angle γ is defined as the angle between the longitudinal axis of the nacelle and the horizontal plane. This definition implies that the nacelle axis is, in general, not orthogonal to the longitudinal axis of the tower and, therefore, not orthogonal to the axis of the tower-nacelle connecting piece $\mathcal{N}_{GO_2}^1$ either. In light of the above, the most complicated step to generate the aerodynamic mesh of the nacelle lies in the connection between the tower-nacelle connector and the nacelle itself, which is done through the curved patch $\mathcal{N}_{GO_1}^2$. Such object is obtained by following the next two steps in order:

1. Generate a typical flat GO_1 -like object with appropriate dimensions.

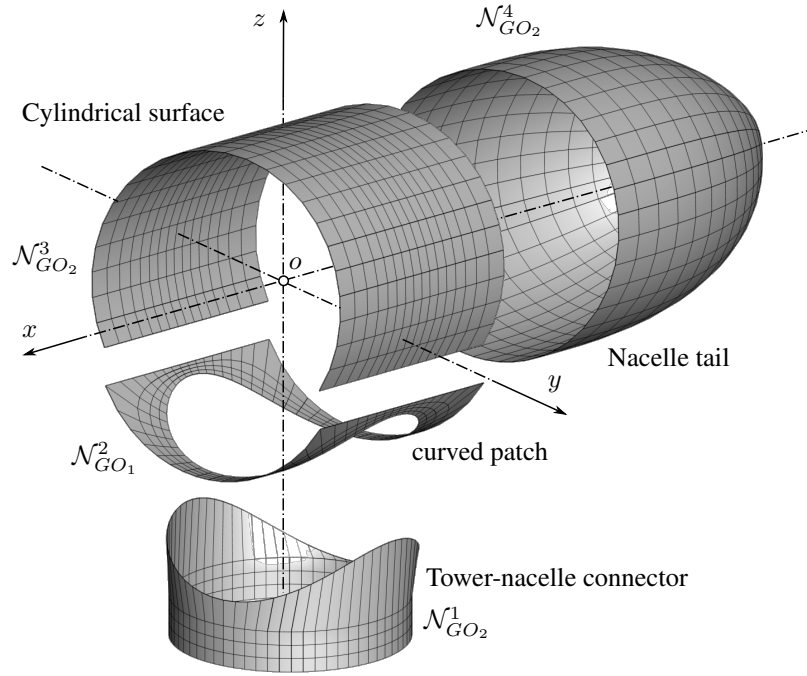


Figure 6. Exploded view of a typical wind turbine nacelle.

225 2. Deform it into a curved surface as shown in Fig. 6. In other words, it means rolling the patch over a “virtual” cylinder representing the nacelle (see Fig. 7).

For the second step, we consider a continuous deformation \mathcal{T}_n that maps each point \mathbf{r} in a connected subset $\mathcal{D} \subset \mathbb{R}^2$ to a point $\mathbf{R} = \mathcal{T}_n(\mathbf{r})$ on a surface in the three-dimensional space \mathbb{R}^3 . Mathematically, $\mathcal{T}_n : \mathcal{D} \subset \mathbb{R}^2 \rightarrow \mathbb{R}^3$ is given by:

$$\mathcal{T}_n(x, y) = x \hat{\mathbf{E}}_1 + R_{N1} \sin\left(\frac{1}{R_{N1}} y\right) \hat{\mathbf{E}}_2 + R_{N1} \cos\left(\frac{1}{R_{N1}} y\right) \hat{\mathbf{E}}_3, \quad (6)$$

230 where R_{N1} is the radius of the cylinder representing the nacelle. It is straightforward to prove that the deformation map \mathcal{T}_n is an *isometric map*. Therefore, it preserves the length of every possible arc of material points on the parametric domain \mathcal{D} . This is true if and only if the Jacobian $D\mathcal{T}_n$ on \mathcal{D} preserves the lengths of vectors in \mathbb{R}^2 in the sense that $\|D\mathcal{T}_n(\mathbf{r})\| = \|\mathbf{r}\|$ for each $\mathbf{r} \in \mathbb{R}^2$. Equivalently, $D\mathcal{T}_n$ must obey $(D\mathcal{T}_n)^T D\mathcal{T}_n = \mathbf{I}_2$, with \mathbf{I}_2 being the identity linear transformation on \mathbb{R}^2 Chen et al. (2018). Once the flat patch has been deformed into a curved patch, an affine transformation (translation and/or rotation)
 235 $\mathcal{A}_n : \mathbb{R}^3 \rightarrow \mathbb{R}^3$ is applied to assemble it with the rest of the nacelle. Thereby, the $\mathcal{N}_{GO_1}^2$ object is obtained by means of the following map composition:

$$\mathcal{N}_{GO_1}^2 = \mathcal{A}_n \circ \mathcal{T}_n(\mathcal{D}). \quad (7)$$



Finally, we need to address the non-smooth connection between the curved patch and the tower-nacelle connector. Such a non-smoothness arises as consequence of two reasons: *i*) the deformation of the original circular hollow cavity (flat patch) into an elliptical cavity (curved patch), and *ii*) the misalignment between the tower longitudinal axis and the hollow axis of the curved patch. For this purpose, we compute in advance the radii of an elliptical hollow in the original flat patch that will ensure a smooth connection between the tower and the deformed curved patch $\mathcal{N}_{GO_1}^2$ (see Fig. 7). Such radii are given by:

$$\begin{aligned}
 r_x &= \frac{R_{N3}}{\cos \gamma}, \\
 r_y &= R_{N1} \sin^{-1} \left(\frac{R_{N3}}{R_{N1}} \right),
 \end{aligned} \tag{8}$$

where R_{N3} is the tower-nacelle connector radius (see Table A.3). When $\gamma = 0$, the radius r_x in (7) is directly the radius of the upper part of the tower (no tilt angle). However, the radius r_y is different from the upper tower radius because of the deformation of the flat patch. Table A.3 in Appendix A provides a summary of the variables associated with the nacelle.

2.2.3 The hub

The aerodynamic mesh of the hub \mathcal{H} is generated as the union of a series of sub-meshes depending on the number of blades of the wind turbine, namely: *i*) blade-hub connectors $\mathcal{H}_{GO_2}^k$ for $k = 1, \dots, N_B$, *ii*) curved patches $\mathcal{H}_{GO_1}^{N_B+k}$ for $k = 1, \dots, N_B$, and *iii*) the nose of the hub $\mathcal{H}_{GO_2}^{2N_B+1}$. All hub components are generated by GO_2 -like entities with the exception of the curved patches, which are of type GO_1 . Fig. 8 shows an exploded schematic of a typical hub for a 3-blade wind turbine.

As before, the most complicated step to generate the aerodynamic mesh of the hub lies in the connection between the blade-hub connector and the hub itself, which is done through the curved patches. Those objects are generated by following a similar procedure as the nacelle:

1. Generate a typical flat GO_1 -like object with appropriate dimensions.
2. Deform it into a curved surface (see Fig. 7).
3. Make N_B copies of this object and place them properly to assemble the rotor.

The deformation of a flat GO_1 -like object into a curved one resembling a part of the hub's surface is performed by means of a continuous isometric mapping $\mathcal{T}_h : \mathcal{D} \subset \mathbb{R}^2 \rightarrow \mathbb{R}^3$ as follows,

$$\mathcal{T}_h(x, y) = x \hat{\mathbf{E}}_1 + R_{H2} \sin \left(\frac{1}{R_{H2}} y \right) \hat{\mathbf{E}}_2 + R_{H2} \cos \left(\frac{1}{R_{H2}} y \right) \hat{\mathbf{E}}_3, \tag{9}$$

where R_{H2} is the radius of the cylinder representing the hub (without considering the blade-hub connectors). Once the flat patch has been deformed into a curved patch, we generated as many copies of the curved patch as the number of blades in the wind turbine. Then, an affine transformation $\mathcal{A}_h^k : \mathbb{R}^3 \rightarrow \mathbb{R}^3$ for $k = 1, \dots, N_B$ is applied to assemble each curved patch with

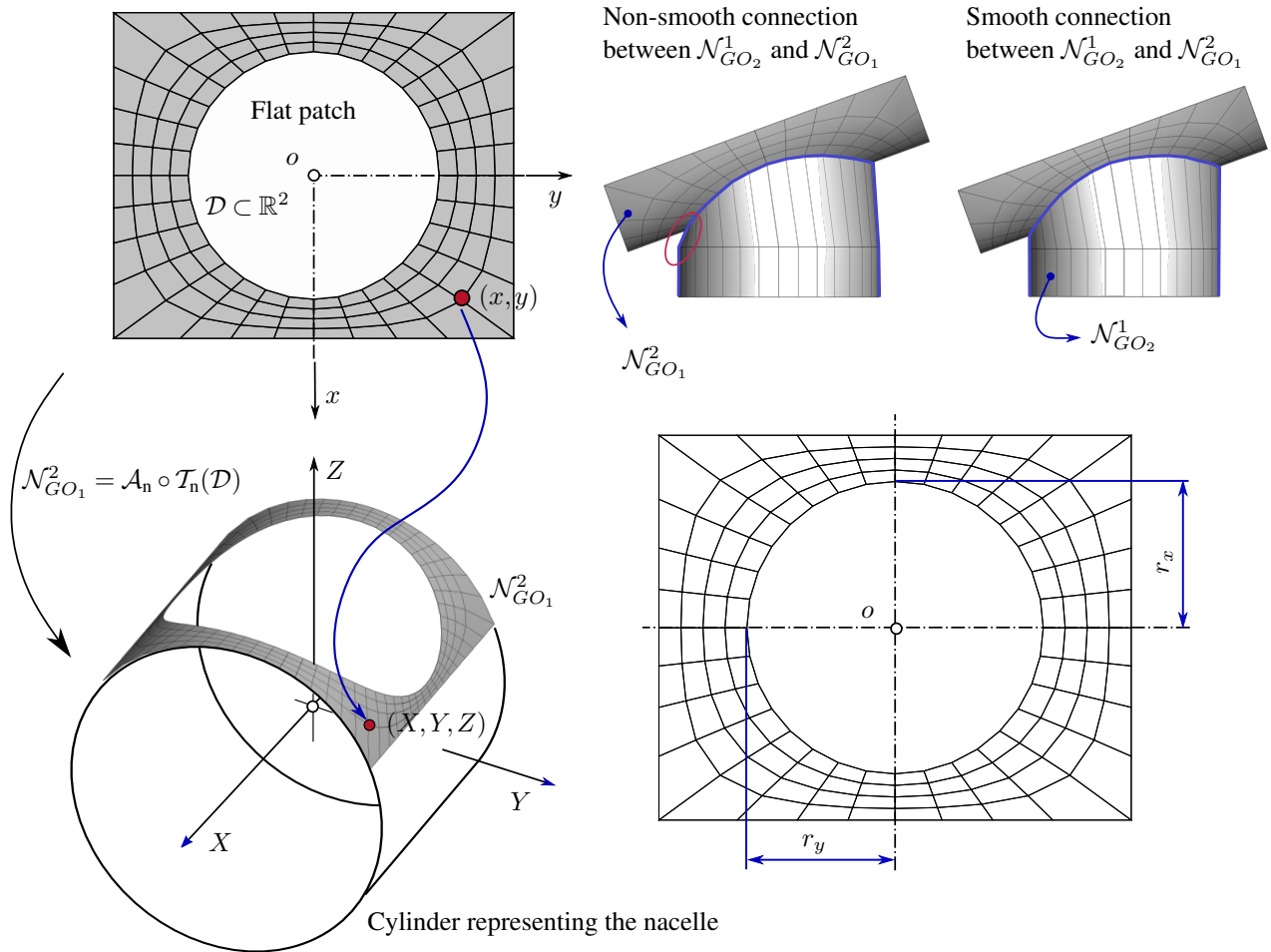


Figure 7. Exploded view of a typical wind turbine nacelle.

the rest of the hub. Thereby, the $\mathcal{H}_{GO_1}^k$ object is obtained by means of the following map composition:

$$265 \quad \mathcal{H}_{GO_1}^k = \mathcal{A}_h^k \circ \mathcal{T}_h(\mathcal{D}), \quad \text{for } k = 1, \dots, N_B. \quad (10)$$

It should be noted that the dimension of the flat patches $\mathcal{H}_{GO_1}^k$ (before deformation) along the y -coordinate (see Fig. 8) depends on the number of blades and the radius of the hub, i.e., $W_{Hy} = 2R_{H1}\pi/N_B$. Finally, the radii of the elliptical hollow in the original flat patch that will ensure a smooth connection between the blade-connector and the deformed curved patch $\mathcal{H}_{GO_1}^k$ are given by:

$$270 \quad r_x = \frac{R_{H3}}{\cos \beta},$$

$$r_y = R_{H2} \sin^{-1} \left(\frac{R_{H3}}{R_{H2}} \right), \quad (11)$$

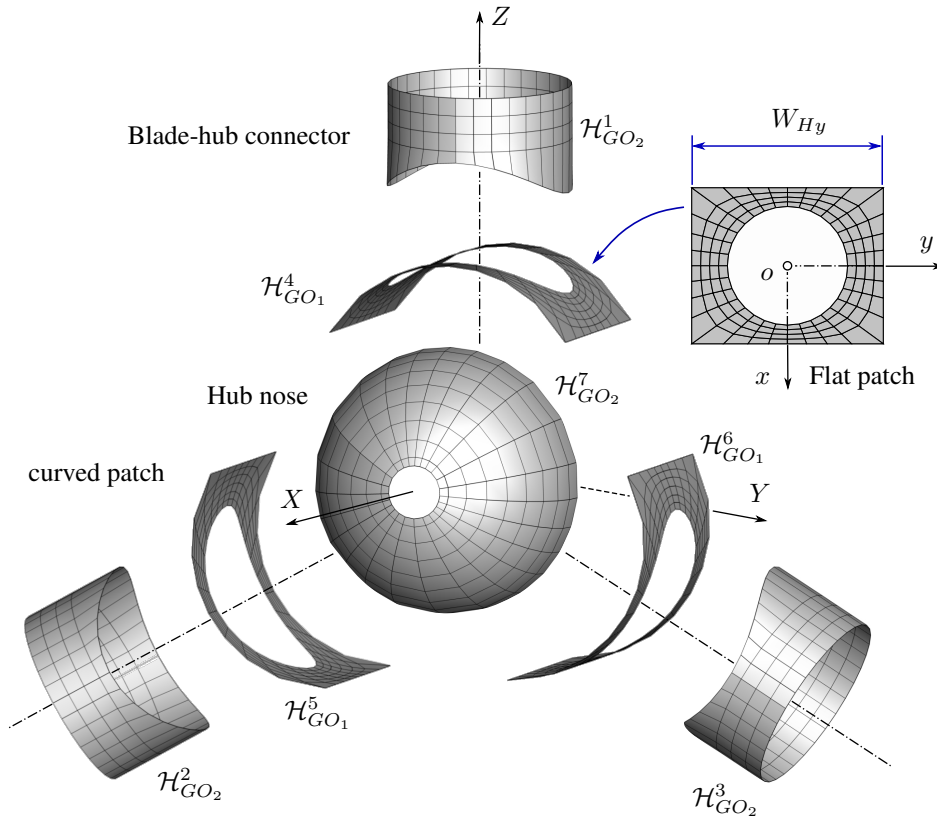


Figure 8. Exploded view of a typical 3-blade wind turbine hub.

where β is the cone angle of the rotor, and R_{H3} is the blade-hub connector radius. When $\beta = 0$, the radius r_x in 11 is directly the radius of the blade-hub connector (no cone angle). Table A.4 in Appendix A provides a summary of the variables associated with the hub.

2.2.4 The blade

275 The aerodynamic mesh of a blade \mathcal{B} is generated as the union of two sub-meshes, namely: *i*) the blade root $\mathcal{B}_{GO_2}^1$, and *ii*) the lifting surface of the blade $\mathcal{B}_{GO_2}^2$. All blade components are generated by GO_2 -like entities.

The mesh generation for wind turbine blades is a non-trivial process because it involves discretizing a three-dimensional surface whose shape changes along its longitudinal axis. Table 3 lists the geometric data that must be provided, as a function of the longitudinal coordinate, to build a three-dimensional wind turbine blade. To simplify what follows and avoid falling
 280 into excessive formalism, let us define B_0 as the set of design parameters of the blade. Fig. 9 presents an example of how such parameters are usually defined along the longitudinal axis of the blade. A good representation of its surface necessarily requires specifying these parameters at “several” points along the blade.

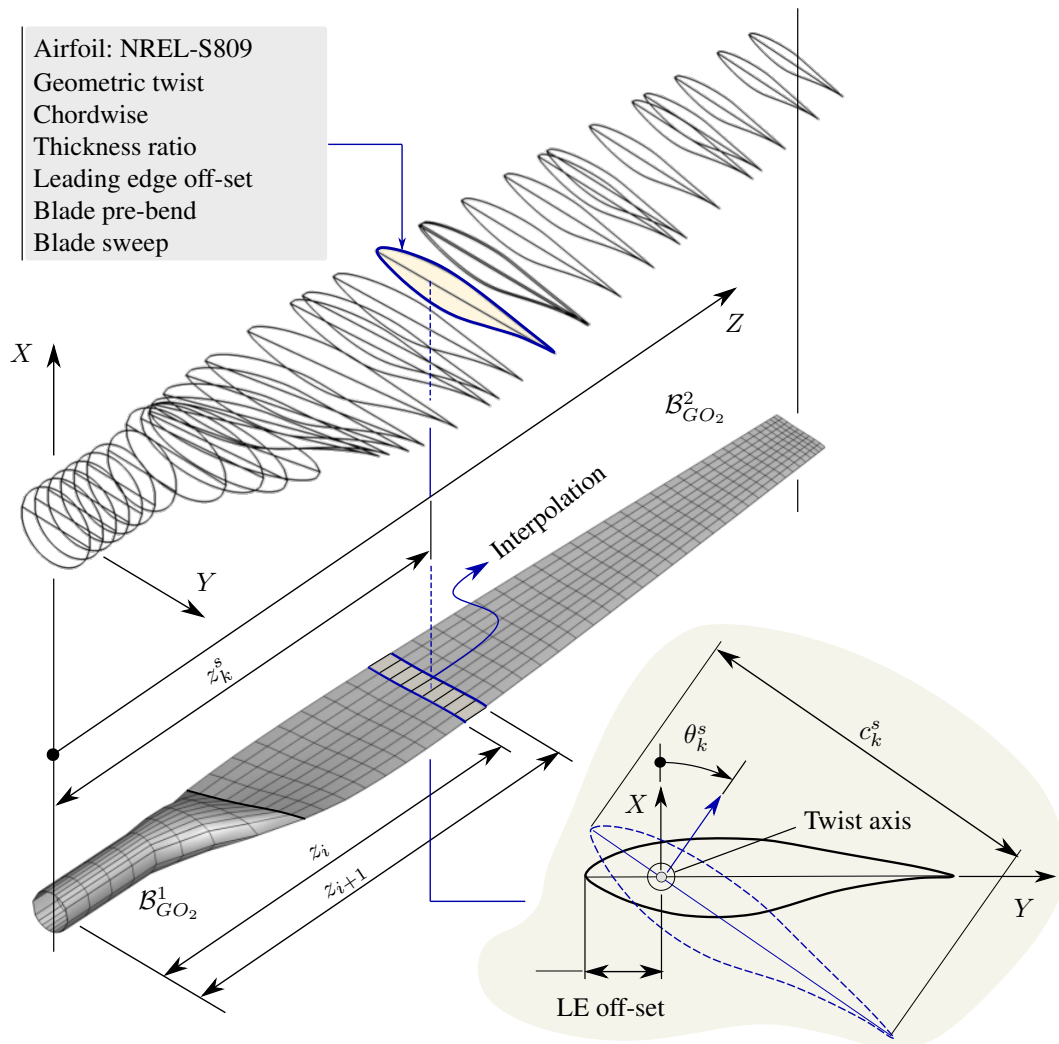


Figure 9. Parameter definition along the blade.

On this basis, the blade is divided into $N_{B2} - 1$ non-uniform intervals such that $[0, L_B] = \cup_{i=1}^{N_{B2}-1} [z_i, z_{i+1}]$ such that $z_{i+1} > z_i$, where L_B is length of the blade, $z_1 = 0$, $z_{N_{B2}} = L_B$, and N_{B2} is the number of nodes along the blade (see Fig. 9). The
 285 geometric parameters at each coordinate z_i are interpolated, according to the provided data B_0 , by using cubic splines. In case of pre-bend and pre-sweep, we have two options, they are either provided by the manufacturer or they can be included by using Zuteck's formula Larwood et al. (2014). The following equation is used to define the sweep and pre-bend,

$$x = x_{tip} \left(\frac{z - z_0}{L_B - z_0} \right)^{\xi_1} \quad \text{and} \quad y = y_{tip} \left(\frac{z - z_0}{L_B - z_0} \right)^{\xi_2}, \quad (12)$$



where y and x are the local distance from the elastic axis (or pitch axis) to the sweep/pre-bend curve, y_{tip} and x_{tip} are the
 290 distance from the pitch axis to the sweep/pre-bend curve at the blade tip, z is the local distance along the blade measured from
 the blade root, z_0 is the position of the beginning of the blade sweep/pre-bend, and ξ is the sweep/pre-bend exponent (see Fig.
 10a).

Table 3. Blade Geometry definition: user-input parameters

Parameter	Description
Blade station, z_k^s	Coordinate of the k -th blade station
Airfoil	Airfoil to be used at the k -th blade station
Geometric twist, θ_k^s	Geometric twist at the k -th blade station, positive clockwise
Chordwise, c_k^s	Chord at the k -th blade station
Thickness ratio	The ratio between the maximum thickness of an airfoil section and its chord length at the k -th blade station
Leading edge off-set	Distance between the twist axis and the leading edge at the k -th blade station (unit chordwise)
Pre-bend, x_k^s	Initial flap-wise bending of the blade at the k -th blade station
Pre-sweep, y_k^s	Initial edge-wise bending of the blade at the k -th blade station

The arc length for all curved blade shapes is equal to the original length of the straight blade, but with a slightly smaller rotor
 radius. The arc length of the blade should be kept the same to avoid blade extension, which will bias results towards longer
 295 blades that produce more power. To this end, we consider the position of an arbitrary point on the elastic axis of the blade at
 the reference configuration to be given by $\mathbf{r}_0 = z \hat{\mathbf{E}}_3$, while the position of the same point at the deformed configuration can be
 expressed as follows,

$$\mathbf{r} = x(z) \hat{\mathbf{E}}_1 + y(z) \hat{\mathbf{E}}_2 + z \hat{\mathbf{E}}_3 + \mathbf{u}, \quad (13)$$

where \mathbf{u} is the displacement vector. For a given coordinate z along the blade, the shortening in the axial direction, u_3 , due to
 300 the arc-length conservation can then be written as,

$$\begin{aligned}
 s(z) &= \int_0^z \|\mathbf{r}'(\eta)\| d\eta, \\
 &= \int_0^z \sqrt{x'^2(\eta) + y'^2(\eta) + (1 + u_3'(\eta))^2} d\eta, \\
 u_3(z) &= \int_0^z \left\{ \sqrt{1 - [x'^2(\eta) + y'^2(\eta)]} - 1 \right\} d\eta,
 \end{aligned} \quad (14)$$

where η is a dummy integration variable, s is the arc-length coordinate along the curved blade, and $(\cdot)'$ stands for derivative
 with respect to η . To obtain the shortening at a given blade section z (last expression in (14)), we enforced the arc-length
 conservation by imposing that the length of the deformed blade must be equal to the original straight blade length, i.e., $s(z) = z$.



305 The blade root is represented as $z = 0$ in (14). The variables x and y represent the local distance from the pitch axis to the sweep and pre-bend curve, respectively. Then, the new nodal z -coordinates associated to the initial partition $[0, L_B]$ are obtained as $z_i^d = z_i - u_3(z_i)$.

Once the new z -coordinates are obtained, we perform a sanity analysis on all curved blades to check that the arc length is close enough to the length of the straight blade. Such analysis is carried out by computing the difference between the original
 310 blade length and the curved blade length,

$$L_B^d = \int_0^{z_c} \sqrt{1 + x'^2(\eta) + y'^2(\eta)} d\eta, \quad (15)$$

where z_c is the tip radius of the curved blade. A script is used to automatically calculate z_c , perform the arc length sanity check, and prepare the blade geometry. In Fig. 10b, we present some examples for sweep and pre-bend blade configurations. Table A.5 in Appendix A provides a summary of the variables associated with the blade.

315 2.2.5 The ground

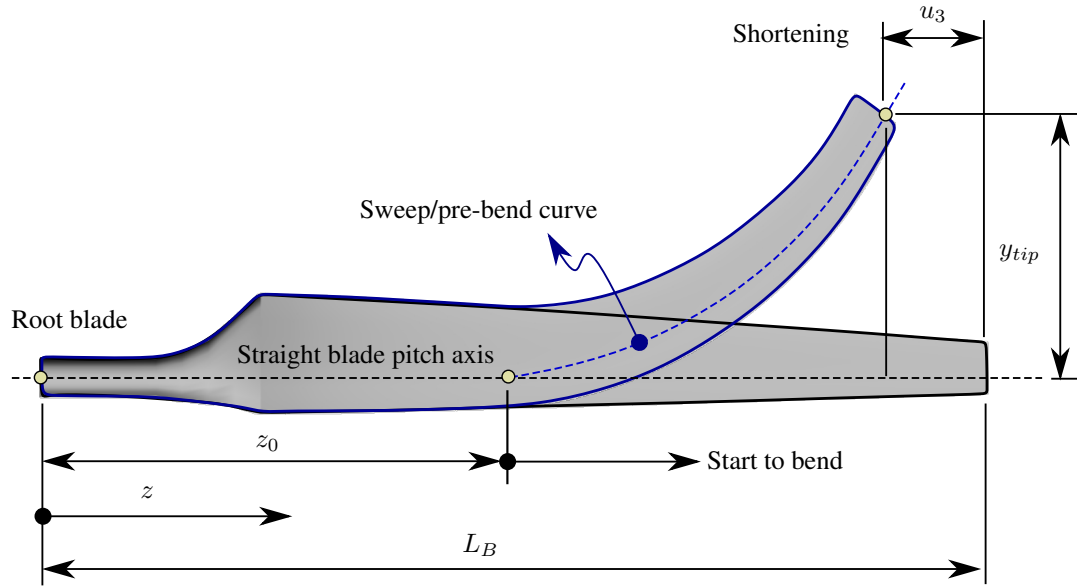
The aerodynamic mesh of the ground \mathcal{G} is generated using only a GO_1 -like object. As input data we need to provide: *i*) the ground-tower connection radius, *ii*) the extent of the ground, namely, the side length of the square representing the ground area, and *iii*) the number of aerodynamic nodes along its radial and tangential directions. Additionally, it is possible to generate an uneven ground by providing a user-defined function to compute the ground elevation or a scattered data set representing the
 320 ground elevation. The last option requires a fitting procedure (regression) to obtain the elevation on the ground aerodynamic mesh. This feature will be discussed in more detail in the computational implementation section. Table A.6 in Appendix A provides a summary of the variables associated with the ground.

2.2.6 Wind turbine assembling

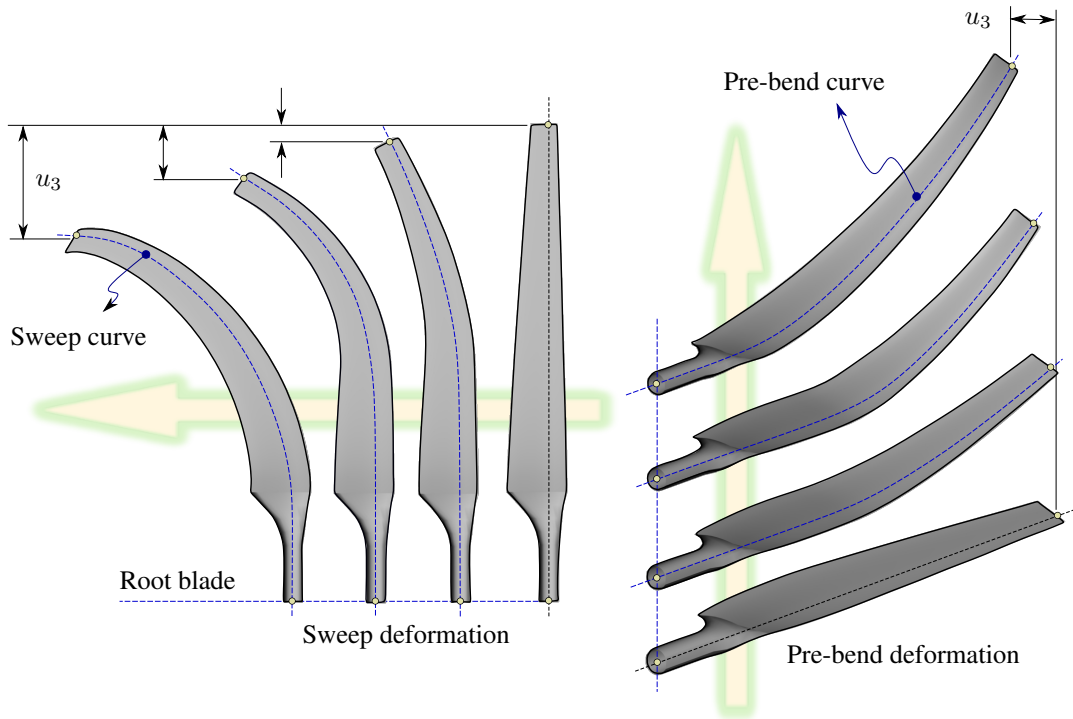
Once all the components for a given wind turbine configuration are generated, the next step is to assemble them to obtain the
 325 complete wind turbine mesh. The code internally calculates all the data required to assemble each turbine within the wind farm. The only information to be provided by the user is: the initial rotor angle, the initial yaw angle, and initial pitch angles. Table 4 lists the data that must be supplied by the user to assemble the turbine. These data are located at the end of each turbine data sheet.

Table 4. Assembling parameters

Variable	Structure field name	Description
θ_y	Yaw0WT	Initial yaw angle [°]
θ_R	Rot0WT	Initial rotor angle [°]
θ_p	Pitch0WT	Initial pitch angle of each blade [°]



(a)



(b)

Figure 10. (a) Parameters that define the wind turbine blade sweep and pre-bend, (b) Sweep and pre-bend blade deformations.



It should be stressed that the the number of pitch angles to be provided must match the number of blades in the rotor, i.e.,
330 $\theta_p \in \mathbb{R}^{N_B}$, and their values can be different from each other. As an example, we present below how the initial angles must be specified to configure a three-blade rotor.

```
0    % Yaw0WT - Initial yaw angle [°]  
0    % Rot0WT - Initial rotor angle [°]  
4,4,4  % Pitch0WT - Initial pitch angle [°]
```

3 Computational implementation

In this section we describe the main aspects associated with the computational implementation of the mesh generator code
335 called *UVLMeshGen* developed at the University of Bergen (Norway) in collaboration with *Universidad Nacional de Río Cuarto* (Argentina). The full code is available in a Github repository Roccia (2023) for public access under a **Creative Commons Attribution 4.0 International License**.

This meshing tool is fully implemented in Matlab[®] and it is intended for generating meshes for onshore and offshore wind farms consisting of horizontal-axis wind-turbines. Among the main features of *UVLMeshGen*, we can mention the following:

- 340
- wind farm meshing,
 - terrain meshing,
 - specification of terrain topography,
 - kinematic processor, and
 - exporting files (Tecplot, UVLM, ...)

345 *UVLMeshGen* provides meshing data into a series of structure variables by using typical FEM-oriented data arrays, such as: nodal coordinate arrays and connectivity arrays. Next, we describe to some extent the organization of the code, description of the main script, important variables, and the features introduced above.

3.1 Code structure

The mesh generator is designed by following a procedural programming paradigm. The software contains two main blocks: *i*)
350 the geometric processor, which is responsible for generating the mesh of each wind turbine component and its assembling; and *ii*) the kinematic processor, which is in charge for computing the kinematics of lifting and non-lifting surfaces. The exporting module, which is responsible for writing output files (Tecplot, input data for UVLM-based codes, etc.), can be added/modified by the user according to his needs. However, the code incorporates an option to export meshes in Tecplot format by default. In Fig. 11 we present a flowchart of *UVLMeshGen*.

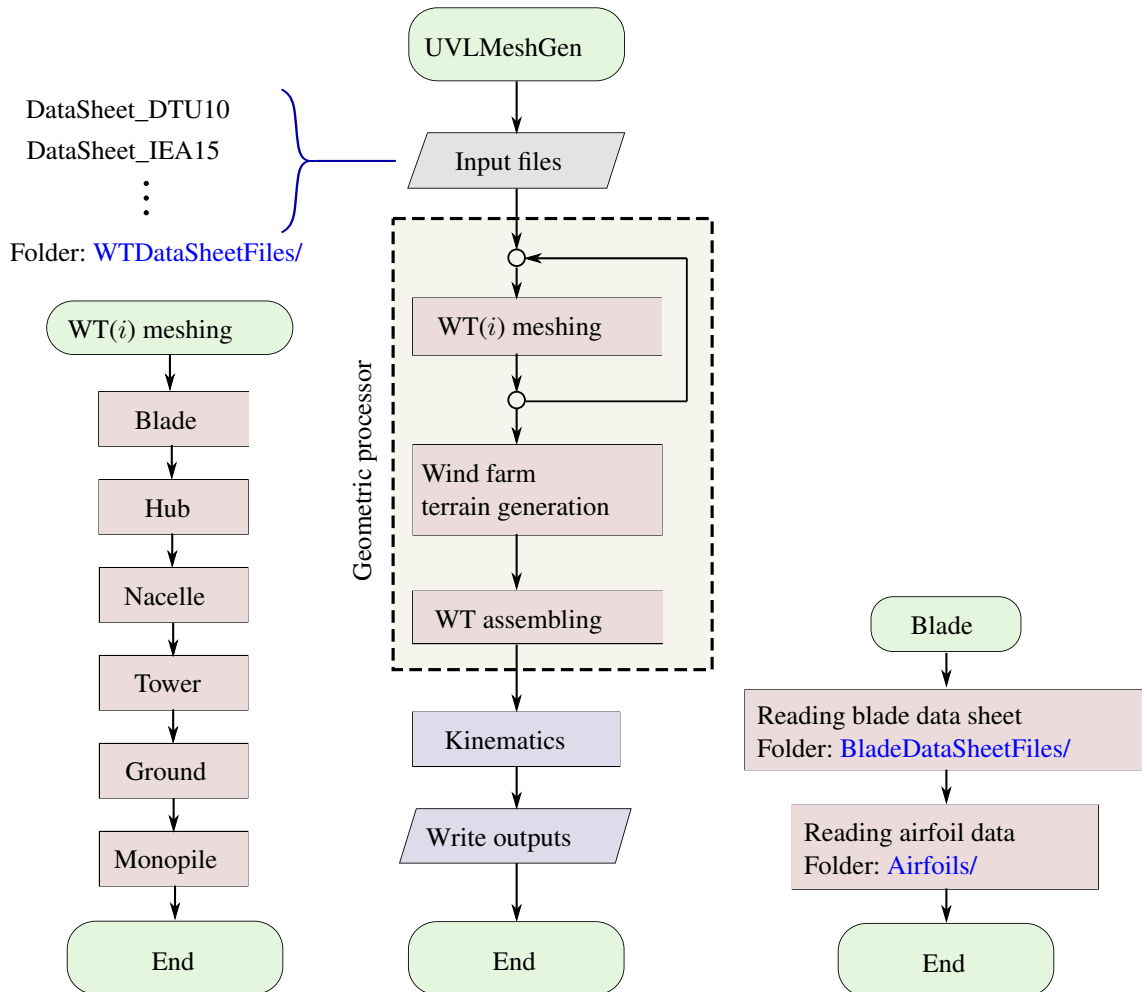


Figure 11. UVLMeshGen flowchart.

355 The input files needed by UVLMeshGen are ASCII-files and user-defined Matlab functions. To keep all the input files clean and separate from the main code, all of them are organized in several folders.

The code starts by loading as many input files as different wind turbines the wind farm contains. These files must be located inside the folder “WTDataSheetFiles/”, and they gather the geometric definition of each wind turbine. Then, the code generates the meshes associated with each wind turbine component. Among them, the blade requires an additional input file containing its complete setup (see Table 3), which must be located inside the folder “BladeDataSheetFiles/”. The blade configuration file also makes reference to the airfoil distribution along its spanwise direction, thus requiring further information about airfoil coordinates. These data are stored inside the folder “Airfoils/”.

Once all the components for each wind turbine have been generated, the code continues with the wind farm terrain, depending on whether it is activated or not in the main script. Then, all wind turbine parts are assembled to shape the final wind farm.



365 The aforementioned processes, namely the generation of wind turbine components, terrain and their final assembly into a wind
 park make up the so-called *Geometric Processor*.

UVLMeshGen also has a kinematics module that is in charge for generating pitch, yaw, and rotor motions. This module is
 general enough to allow any kinematics to be prescribed by the user through custom user-defined functions. Such feature is
 very useful to investigate the aerodynamic performance of wind turbines. To write the outputs, users can either select some of
 370 the file formats included by default or provide their own scripts to export data.

3.2 Main script

The code is executed through a main script which contains a set of general options, such as: wind farm layout, terrain elevation,
 wind turbine kinematics, and output files. In Table 5 we present a brief description of the variables to be specified in the main
 script.

Table 5. Main script variables - general options

Variable	Description
NumWT	Number of wind turbines (integer variable, denoted N_{WT})
EQWT_FLAG	Homogeneous wind turbine farm option (string variable). The available options are either “ON” or “OFF”
WTNames	Name of the files containing the setup of each turbine and its (X, Y, Z) -location in the wind farm (cell array)
ProjectName	Name to be used to save all the output files, such as: Tecplot files and mesh report, among others (string variable)
GroundDivision	(X, Y) division of the wind farm terrain (cell array)
Ground_FLAG	Options associated with the wind farm terrain and terrain elevation (cell array)
Kinematic_FLAG	Options associated with wind turbine kinematics (cell array)
OPT_FLAG	Option associated with exporting files (cell array)

375 **WTNames:** this is a cell array variable of dimension $N_{WT} \times 4$. The first column contains the file names associated with
 the configuration of each wind turbine in the wind farm. The last three columns contain the (X, Y, Z) -coordinates of each
 wind turbine. As an example, let us consider a wind farm made up of four different wind turbines ($N_{WT} = 4$). Under these
 assumptions, the variable WTNames could take the following values:

```
WTNames = {'DataSheet_DTU_10MW.DAT', 0.0, 0.0, 0.0
           'DataSheet_IEA_15MW.DAT', -100.0, 100.0, 0.0
           'DataSheet_Sandia01.DAT', -120.0, -120.0, 0.0
           'DataSheet_Sandia01.DAT', 100.0, -100.0, 0.0}.
```



380 **EQWT_FLAG**: this is a string variable which can take only two values: ON or OFF. If the value ON is used, the wind farm will consist of only one type of wind turbine. The setup of said turbine corresponds to the one specified in the first row of the variable `WTNames`. However the number of rows of `WTNames` must still be equal to the number of turbines considered in `NumWT`. This is because the wind turbines will be placed within the wind farm by extracting the coordinates from the variable `WTNames`.

385 **GroundDivision**: this is a cell array variable of dimension 2×1 . The cell `GroundDivision{1,1}` contains the coordinates of the patches into which the terrain will be divided along the X direction. In a similar way, the cell `GroundDivision{2,1}` contains the coordinates of the patches into which the terrain will be divided along the Y direction. The number of patches along the X and Y directions are determined as $\dim(\text{GroundDivision}\{\cdot,1\}) - 1$.

To ensure a smooth terrain surface with a regular discretization of elements, it is recommended to consider one patch per turbine in the wind farm. The dimensions of the patch must be large enough to accommodate the ground-tower coupling. Once the surface of the terrain is divided, the code will automatically determine where the turbines are located, it will generate the corresponding ground-tower coupling, and in those patches without turbines, the code will generate a rectangular grid. As an example, let us consider the wind farm introduced above (see variable `WTNames`). For this wind farm layout, a suitable terrain division could be as follows:

390
$$\text{GroundDivision} = \{ [180, 60, -60, -180]$$

395
$$[180, 60, -60, -180] \},$$

from which it is clear that three patches were considered along both directions, i.e., nine patches in total. In Fig. 12 we present a schematic intended to explain how the terrain division is performed and the reference frame used.

Ground_FLAG: this is a cell array variable of dimension 1×6 . All the cells contained in this array are of type string and they specify whether or not to generate the wind farm terrain. In addition, this variable allows to configure the terrain elevation and what options will be used to generate it. The reader is referred to Subsection 3.4 for a more detailed description of this feature.

Kinematics_FLAG: this is a cell array variable of dimension 1×5 . All the cells contained in this array are of type string and they specify whether or not kinematics associated with different wind turbine components are generated (e.g., yaw motion, pitch motion and/or rotor motion). Furthermore, this variable allows configuring the time step to be used for the kinematics when considering heterogeneous wind farms. The reader is referred to Subsection 3.5 for a more detailed description of this feature.

OPT_FLAG: this is a cell array variable of dimension 1×2 . All the cells contained in this array are of type string and they specify whether or not the generated meshing data will be exported. This option consists of two fields as follows:

$$\text{OPT_FLAG} = \{ 'ON', 'MyOutput' \},$$



connectivity arrays associated with the entire wind farm discretization. The third variable contains the wind farm kinematics; namely, positions and velocities of the entire wind farm mesh for the stipulated simulation time grid. The last variable contains all data associated with the wind farm terrain.

- 425 – **WIND_TURBINE**: this variable is indexed by the number of wind turbines within the wind park, i.e., $\text{WIND_TURBINE}(i)$ for $i = 1, \dots, N_{WT}$. In Table B.1 in Appendix B, we list the main fields associated with **WIND_TURBINE** structure. If any component of the wind turbine is disabled during the geometric modeling, the field associated with it is assigned the “empty value”.
- **CONNECT**: as before, this variable is indexed by the number of wind turbine within the wind park. In Table B.2 in
430 Appendix B, we list the main fields associated with **CONNECT** structure.
- **GROUND_FARM**: this variable contains only information regarding the wind farm terrain. There is no kinematics associated with the terrain since it is motionless, so its position is the same over time, and therefore the velocities at the control points are zero for all t . In Table B.3 in Appendix B, we list the main fields associated with **GROUND_FARM** structure. The field $\text{GROUND_FARM.PATCH}(i)$ for $i = 1, \dots, N_{Gp}$, where N_{Gp} is the number of patches into which the terrain
435 was divided, contains nodal coordinates and connectivities, among other data.
- **KINEMATICS**: this variable is indexed by the number of simulation time steps used by the kinematics processor, i.e., $\text{KINEMATICS}(i)$ for $i = 1, \dots, N_{\Delta t}$, where $N_{\Delta t}$ is the number of time steps. As fields, this variable contains: *i*) $\text{KINEMATICS}(i).\text{GroundFarm.PATCH}(k)$ for $k = 1, \dots, N_{Gp}$, and *ii*) $\text{KINEMATICS}(i).\text{WT}(j)$ for $j = 1, \dots, N_{WT}$. Although the terrain is motionless, $\text{KINEMATICS}(i).\text{GroundFarm}$ stores the nodal coordinates, CP coordinates and
440 CP velocities (which are zero) over time. This decision on the storage of terrain data is based on a potential future implementation of “terrain motion” to simulate the sea surface and the effects of waves on offshore wind turbines. The fields associated with the second structure, $\text{KINEMATICS}(i).\text{WT}(j)$, are listed in Table B.4 in Appendix B.

3.4 Wind farm terrain processor

This module is in charge of generating the wind farm terrain. All necessary parameters are introduced via the `Ground_FLAG`
445 cell array variable located in the main script. As previously mentioned, this variable consists of six cells as follows:

```
Ground_FLAG = {'ON', 'ON', 'userfunction', 'MyGround',  
              'GroundData.DAT', 'poly23'},
```

where the first and second cells admit two values $\{\text{ON}, \text{OFF}\}$ indicating whether the wind farm terrain generation is activated or not and whether the terrain elevation feature is enabled or not, respectively. The third cell supports two different keywords $\{\text{'userfunction'}, \text{'externaldata'}\}$, which specify whether the terrain elevation will be generated via some user-
450 defined function, or whether it will be generated by fitting a scattered terrain data set. The fourth and fifth cells specify the



name of the user-defined function and the name of the file containing the terrain data set, which should be placed inside the “Terrain Data/” folder. The mesher will use either the function or the data set according to the option specified in the third cell. The last cell specifies the fit type to use if `externaldata` is selected. Internally, the mesher uses the Matlab[®] intrinsic function “`fit`” to fit a surface to the data provided by the external file. Any fitting option accepted by `fit` can be
455 specified as a valid option in `Ground_FLAG`.

The user-defined function for generating the terrain elevation must receive two inputs: *i*) an array of dimension $N_{WF} \times 3$ containing the nodal coordinates of the flat wind farm terrain, and *ii*) the number of nodes of the wind farm terrain, N_{WF} . The terrain coordinates within the input array are organized as follows: *X*-coordinates (first column), *Y*-coordinates (second column), and *Z*-coordinates (third column). The user can impose/calculate any elevation profile on the ground (coordinates
460 *Z*) as long as it does not present abrupt changes. As output, the function only needs to provide an array of coordinates of dimension $N_{WF} \times 3$, where the third column contains the *Z*-coordinates modified according to the elevation model proposed by the user. As an example, we provide below a very simple user-defined function that allows to impose a terrain elevation profile.

```
function C = MyTerrainLevel (XYZ, NWF)
Ymin = min(XYZ(:,2));
Ymax = max(XYZ(:,2));
DD = Ymax - Ymin;
C = XYZ;

A = [Ymin^2 Ymin 1; Ymax^2 Ymax 1; 2*Ymin 1 0];
F = [0; DD/6; 0];
Coef = A\F;

for i = 1:NWF
    C(i,3) = Coef(1)*C(i,2)^2 + Coef(2)*C(i,2) + Coef(3);
end
```

465 Fig. 13 shows the elevation of the ground surface generated by using a parabolic and a sinusoidal profile. The ground surface corresponding to the parabolic profile was generated using the user-defined function introduced above. As can be seen, the elevation profile does not present any type of abrupt changes or jumps.

When the option ‘`externaldata`’ is chosen, an external ASCII file containing (*X*,*Y*,*Z*)-coordinates of points on the ground must be provided. The amount/quality of the points considered should be large/good enough to ensure that the fitted

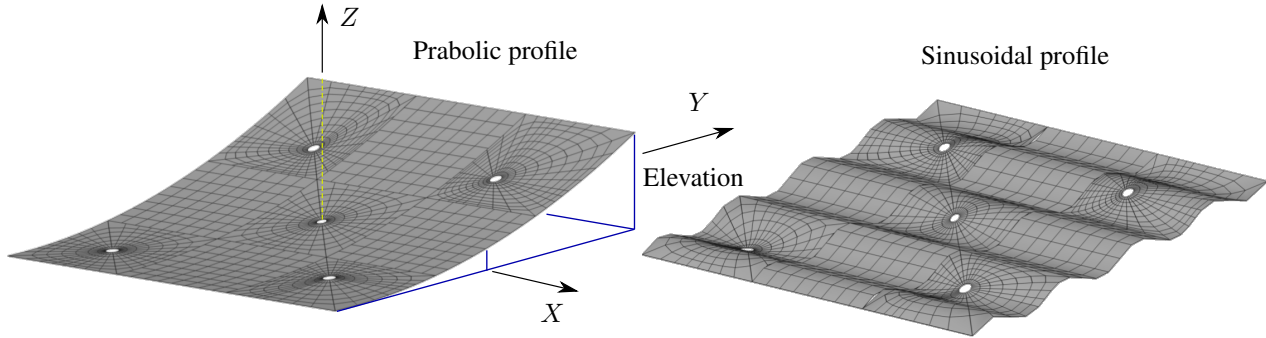


Figure 13. Example of wind farm terrain elevations.

470 surface renders a realistic elevation profile. Once the fitting process is done, the resulting surface equation will be used to find the elevation for a given nodal terrain coordinate (X, Y) . The data must be provided in three columns: X -coordinates (first column), Y -coordinates (second column), and Z -coordinates (third column).

3.5 Kinematic processor

This module is in charge of generating the kinematics for the entire wind farm. As before, all necessary parameters are introduced
 475 via the `Kinematic_FLAG` cell array variable located in the main script. As previously mentioned, this variable consists of five cells as follows:

```
Kinematic_FLAG = {'ON', 'RotorOFF', 'YawOFF', 'PitchOFF', 'min'};
```

where the first cell admit two values $\{'ON', 'OFF'\}$ indicating whether the wind farm kinematics is enabled or not. The second through fourth cells allow us to specify whether rotor, yaw, and pitch kinematics are enabled or not. Each of these cells
 480 admits two values: $\{'RotorON', 'RotorOFF'\}$, $\{'YawON', 'YawOFF'\}$, and $\{'PitchON', 'PitchOFF'\}$.

When considering a wind farm, it may happen that it is composed of different types of turbines (heterogeneous wind farm), which can in turn result in very different aerodynamic grids (e.g., large differences in the size of aerodynamic panels). In UVLM-based codes it is customary to define characteristic magnitudes for computing force coefficients. Typically they are: the characteristic density ρ_C , the characteristic length L_C , the characteristic velocity V_C , and the characteristic time T_C which
 485 is obtained as $T_C = L_C/V_C$. `UVLMeshGen` offers two options for setting the characteristic length. This can be either provided by the user or computed by using a default internal procedure. If the automatic option is selected, L_C is calculated based only on the discretization of the blade lifting surface as follows,

$$L_C = \sqrt{\frac{\sum_{i=1}^{N_{LS}} A_i}{N_{LS}}}, \quad (16)$$



where N_{LS} is the number of panels on the blade lifting surface, and A_i is the surface area of the i -th panel belonging to
 490 the lifting surface. Regarding the characteristic velocity, it is usually set to be the magnitude of the free-stream velocity, i.e.,
 $V_C = V_\infty$.

Under the above definitions, it is clear that the time step used by standard UVLM codes based on time-stepping schemes
 directly depends on the spatial discretization of the blade, i.e., how fine or coarse the aerodynamic grid is. This fact is particu-
 larly important for generating the kinematics of heterogeneous wind farms. In a scenario like this, each wind turbine will have
 495 its own time step, which greatly complicates the aerodynamic simulation of the wind farm. A simple way to overcome this
 problem is to define an unique time step for the entire wind farm, Δt_{wf} . Clearly, there are several ways to define such Δt_{wf} ,
 for instance: *i*) a minimum time step, *ii*) a maximum time step, or *iii*) an average among the time steps associated with different
 wind turbines. These three options are available in UVLMeshGen by specifying 'min', 'max', or 'average' in the last
 cell of `Kinematic_FLAG`. According to the option selected, Δt_{wf} is computed as follows,

$$\begin{aligned}
 \{ ' \text{min}' \} &\longrightarrow \Delta t_{wf} = \min \{ \Delta t_1, \Delta t_2, \dots, \Delta t_{N_{WT}} \} \\
 \{ ' \text{max}' \} &\longrightarrow \Delta t_{wf} = \max \{ \Delta t_1, \Delta t_2, \dots, \Delta t_{N_{WT}} \} \\
 \{ ' \text{average}' \} &\longrightarrow \Delta t_{wf} = \frac{1}{N_{WT}} \sum_{i=1}^{N_{WT}} \Delta t_i,
 \end{aligned}
 \tag{17}$$

500

where Δt_i is the time step associated with each wind turbine in the farm. In Table 6, we provide a summary of further kinematic
 variables that must be specified in each wind turbine sheet file (variable `WTNames` described in Subsection 3.2).

Table 6. Kinematic variables

Variable	Structure field name	Description
*	NameRot	User-defined function name containing the rotor kinematics
*	NameYaw	User-defined function name containing the yaw kinematics
*	NamePitch	User-defined function name containing the pitch kinematics
L_C	UVLM_LC	Characteristic length (0: L_C is automatically computed)
V_C	UVLM_VC	Characteristic velocity
$N_{\Delta t}$	UVLM_Steps	Number of time steps

User-defined functions must be placed inside the “Kinematic Files/” folder. The mesher will use such m-files func-
 tions to generate the kinematic laws for rotor, yaw and pitch depending on whether such options are enabled in `Kinematic_FLAG`
 505 or not. Each of these functions must receive three inputs: *i*) number of time steps, *ii*) time step, and *iii*) initial angle. For func-
 tions related to the rotor and yaw kinematics, the third argument is a scalar variable that specifies their initial angles. In case
 of pitching, such a variable is a vector of dimension N_B containing the initial pitch of each blade in the rotor. As output, the
 function must provide two arrays of dimension $1 \times N_{\Delta t}$ for rotor and yaw kinematics, and $N_B \times N_{\Delta t}$ for pitch kinematics. The



510 first output variable contains the angle time-series and the second one contains the time derivative of the angle time series. As an example, we provide below a very simple user-defined function which allows to impose a harmonic yaw motion on a rotor wind turbine.

```
function [A, DA] = MyYaw (NTS, DT, A0)
A0 = A0 * pi / 180;
YH = 60 * pi / 180;
YW = 0.35;
T = linspace(0, NTS*DT, NTS+1);

A = A0 + YH * sin (YW * T);
DA = YH * YW * cos (YW * T);
```

It should be noted that all input angles are in degrees.

4 Unsteady vortex-lattice method

515 In this section, we present a brief review of the unsteady vortex-lattice method in order to highlight the relationship between the geometric modeling introduced in previous sections and the data needed by UVLM-based solvers when it comes to aerodynamic simulations of complex aeronautical/mechanical engineering applications; here wind energy farms in particular.

According to Hente et al. (2022); Preidikman (1998); Katz and Plotkin (2001), in UVLM-based computational implementations, the continuous bound-vortex sheets are discretized into a lattice of short, straight vortex segments of circulation $\Gamma(t)$.
520 Such segments divide $\partial\mathcal{B}$ into a finite number of elements B_k (also called panels or boundary elements). The wakes shed from the separation zones (trailing edges (TE), wing- or blade-tips, and leading edges (LE)) are also represented by vortex lines. In Fig. 14 we present a schematic representation of the vortex lattices for the hub-nacelle assembly of a wind turbine.

Following Hente et al. (2022), the complete boundary of an aeronautical/mechanical system is geometrically decomposed into a finite set of boundary elements $\mathcal{A}_i = \{B_k^i\}$, such that,

$$525 \quad \mathcal{A} = \bigcup_{i \in S_B} \mathcal{A}_i \quad \text{and} \quad \mathcal{A}_i = \bigcup_{k \in S_i} B_k^i, \quad (18)$$

where $S_B = \{1, 2, \dots, N_B\}$, N_B is the number of bodies, $S_i = \{1, 2, \dots, N_{pb_i}\}$, and N_{pb_i} is the number of panels associated with each aerodynamic subgrid \mathcal{A}_i . Then, the total number of panels used to discretize the whole surface \mathcal{A} is calculated as $N_{pb} = \sum_{i=1}^{N_B} \text{card}(S_i)$.

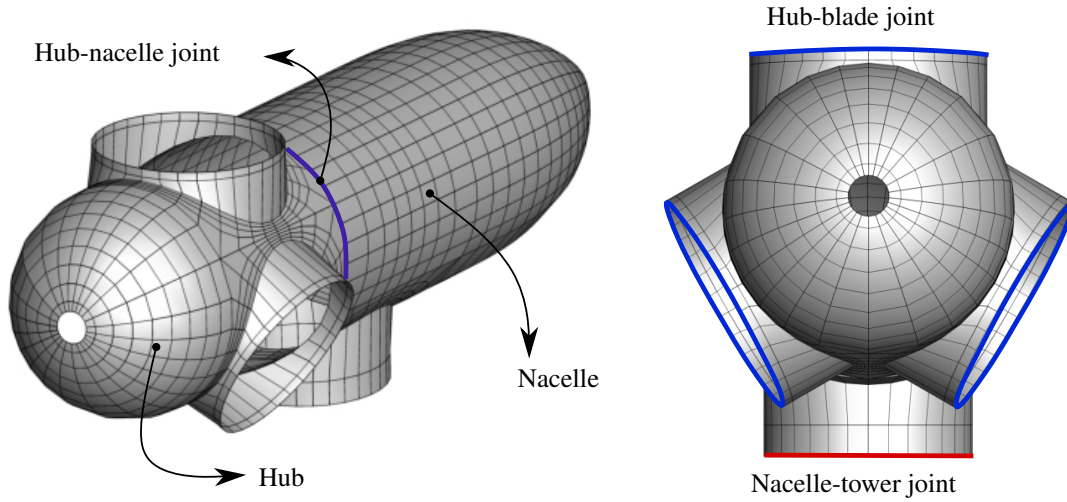


Figure 14. Vortex lattice associate with the hub-nacelle assembly.

It is well known that UVLM-solvers strongly depend on the quality with which lifting and non-lifting surfaces are represented. Wind turbines, and even more so wind farms, are characterized by very complex geometries in general (rotor, blades, terrain topography, etc.), and therefore robust and precise meshing processes are needed to ensure a correct estimation of aerodynamic loads. In this sense, it has been found that the geometric entities GO_1 and GO_2 , described in Section 2, allow to generate all the grids and subgrids associated with sets \mathcal{A}_i .

As mentioned above, the edges of each B_k^i are represented by straight, finite vortex segments of circulation $\Gamma(t)$, whose contribution to the velocity field are computed through a discrete version of the Biot-Savart law,

$$\mathbf{V}(\mathbf{r}, t) = \frac{\Gamma(t)}{4\pi} \frac{(\mathbf{r}_1 \times \mathbf{r}_2) (\|\mathbf{r}_1\| + \|\mathbf{r}_2\|)}{\|\mathbf{r}_1\| \|\mathbf{r}_2\| (\|\mathbf{r}_1\| \|\mathbf{r}_2\| + \mathbf{r}_1 \cdot \mathbf{r}_2) + (\delta_c \|\mathbf{u}\|)^2}, \quad (19)$$

where \mathbf{r}_1 and \mathbf{r}_2 are the position vectors of the point where the velocity is being evaluated relative to the ends of the straight vortex segment, $\mathbf{u} = \mathbf{r}_1 - \mathbf{r}_2$, and δ_c is a cut-off parameter, which is introduced to remove its singular kernel. Although introducing the term $(\delta_c \|\cdot\|)$ into Eq. (19) is interpreted as essentially an ad-hoc technique Chorin (1994); Garrel (2003), it has been proven to work satisfactorily well in practice.

4.1 Aerodynamic influence coefficients

In UVLM-based codes, the non-penetration condition is imposed at the geometric centres of each B_k^i (the so-called control or collocation points, CPs), resulting in a linear system of algebraic equations (usually with time-varying coefficients). The unknowns are the circulations around the individual bound vortex segments; however, the linear system can be rewritten in terms of vortex ring circulations $G_j(t)$, thus reducing the size of the problem Hente et al. (2022). Under these assumptions, the



linear system takes the following form:

$$\sum_{j=1}^{N_{pb}} a_{ij}(t) G_j(t) + [\mathbf{V}_\infty + \mathbf{V}_W(\mathbf{r}_i, t) - \mathbf{V}_S(\mathbf{r}_i, t)] \cdot \hat{\mathbf{n}}_i(t) = 0, \quad i = 1, 2, \dots, N_{pb},$$

$$\mathbf{A}(t)\mathbf{G}(t) = \mathbf{RHS}(t), \tag{20}$$

where $a_{ij}(t)$ are the aerodynamic influence coefficients, $\hat{\mathbf{n}}_i$ is the unit vector normal at the i -th control point, \mathbf{V}_W is the velocity induced by the free-vortex lattice, \mathbf{V}_S is the velocity of the solid, \mathbf{V}_∞ is the free-stream velocity, $\mathbf{A}(t)$ is the aerodynamic influence matrix, $\mathbf{G}(t)$, and $\mathbf{RHS}(t)$ is the right hand side which collects the contributions of the wake, free-stream and body velocities along the normal direction at each CP.

As it can be observed in (20), solving for the unknown circulations requires knowing the body velocities \mathbf{V}_S at each B_k^i control point. Such velocities depend on the kinematics imposed on the rotor (including yaw and pitch motions, if any), substructure kinematics, and sea level surface motions for offshore wind turbines. Consequently, the position and velocity data provided by the kinematic module of the UVLMeshGen (described in Subsection 3.5) play a fundamental role in developing high-quality aerodynamic simulations of arbitrary onshore/offshore wind farms.

4.2 Wake convection

In order to formalize the convection process, let us consider \mathcal{V}_i for $i = 1, \dots, N_W$ be a set of panels $\mathcal{V}_i = \{L_k^i\}$ representing the wake shed from SZs of $\mathcal{A}_j \in \mathcal{A}$, such that,

$$\mathcal{V} = \bigcup_{i \in S_W} \mathcal{V}_i \quad \text{and} \quad \mathcal{V}_i = \bigcup_{k \in W_i(t)} L_k^i, \tag{21}$$

where $S_W = \{1, 2, \dots, N_W\}$, $N_W \leq N_B$ is the number of lifting surfaces, $W_i(t) = \{1, 2, \dots, N_{pw_i}(t)\}$, and $N_{pw_i}(t)$ is the number of vortex rings in \mathcal{V}_i . Then, the total number of free-vortex rings at time t is determined as $N_{pw}(t) = \sum_{i=1}^{N_W} \text{card}(W_i(t))$.

Once the circulations $G_j(t)$ are calculated, the wakes are convected to their new positions and new vortex segments are propagated into the free-vortex lattices. Because all the quantities involved in the convection are functions of time, the question of which instantaneous quantities to use in the approximation is raised. There are several options; for example, one can use the quantities that were calculated at the previous time step, the present time step, or their averaged values for the two time steps. In all cases except the first, iterations are needed, which increase the computational cost. Kandil et al. (1976) showed that explicit one-step methods are stable, and there are little differences in the computed results when compared with higher-order procedures. In this respect, here we use an explicit first-order method to propagate the wake,

$$\mathbf{r}_{\text{node}}(t + \Delta t) \approx \mathbf{r}_{\text{node}}(t) + \mathbf{V}_{\text{node}}(t)\Delta t, \quad \text{node} = 1, \dots, N_{nw}(t), \tag{22}$$



where the subscript “*node*” is introduced to refer to the corners of a vortex segment, $N_{nw}(t)$ is the number of aerodynamic nodes in \mathcal{V} , and Δt is the time step. The vector $\mathbf{V}_{\text{node}}(t)$ collects the contributions from all surface vortex rings B_k^i , all free-vortex rings L_j^i , and the free-stream velocity.

4.3 Aerodynamic loads

575 Among the several procedures proposed in the literature for computing aerodynamic loads by using the UVLM, we can mention the Joukowski approach Simpson et al. (2013); Lambert and Dimitriadis (2017), the Katz approach Katz and Plotkin (2001); Lambert and Dimitriadis (2017), and an alternative formulation based on the Katz method developed at Virginia Tech (VT) Preidikman (1998). Here we present a quick review of the VT approach for predicting aerodynamic forces.

The VT approach is similar to that proposed by Katz. It computes the pressure jump across the bound-vortex lattice by using
 580 the Bernoulli equation for unsteady flows,

$$\frac{Dp}{\rho} = [(\partial_t \varphi + \partial_t \psi)|_U - (\partial_t \varphi + \partial_t \psi)|_L] + \frac{1}{2} (\mathbf{V}_U \cdot \mathbf{V}_U - \mathbf{V}_L \cdot \mathbf{V}_L), \quad (23)$$

where Dp is the pressure jump, ρ is the fluid density, $\partial_t(\cdot)$ stands for partial time derivative, $\mathbf{V}_U = (\nabla \varphi + \nabla \times \boldsymbol{\Psi})|_U$, $\mathbf{V}_L = (\nabla \varphi + \nabla \times \boldsymbol{\Psi})|_L$, $\nabla(\cdot)$ is the Nabla operator in \mathbb{R}^3 , φ is a scalar potential, $\boldsymbol{\Psi}$ is a vector potential, and ψ is another scalar potential such as $\nabla \times \boldsymbol{\Psi} = \nabla \psi$. The component of the velocity field coming from the scalar potential is irrotational while any
 585 vorticity contribution to it is captured by the vector potential component.

After some algebraic manipulations, the pressure jump for the k -element in \mathcal{A} can be expressed as follows,

$$Dp_k = \rho [\mathbf{V}_k^m - \mathbf{V}_k] \cdot \Delta \mathbf{V}_k + \rho \frac{G_k(t) - G_k(t - \Delta t)}{\Delta t}, \quad (24)$$

where $\mathbf{V}_k^m = \mathbf{V}_{B,k} + \mathbf{V}_{W,k} + \mathbf{V}_{\infty,k}$ is the “mean” velocity which does not recognize the presence of the local vorticity, and $\Delta \mathbf{V}_k$ represents the jump in the tangential velocity across B_k . Finally, the vector force on B_k , \mathbf{F}_k , is obtained as the product
 590 of (24) times the element area times the normal unit vector at CP_k ,

$$\mathbf{F}_k = Dp_k^d A_k \hat{\mathbf{n}}_k. \quad (25)$$

For more details about the theory as well as implementations aspects related to the UVLM the reader is referred to Preidikman (1998); Rocca et al. (2013); Verstraete et al. (2023)

5 Numerical Results

595 In this section, we present a series of results to show the capabilities of the mesh generator developed here to build arbitrary wind turbines and wind farms UVLM meshes. To this end, we use the UVLMeshGen along with the VLMSim to reproduce several standard results in the field of wind energy. Furthermore, we present some numerical simulations related to well-

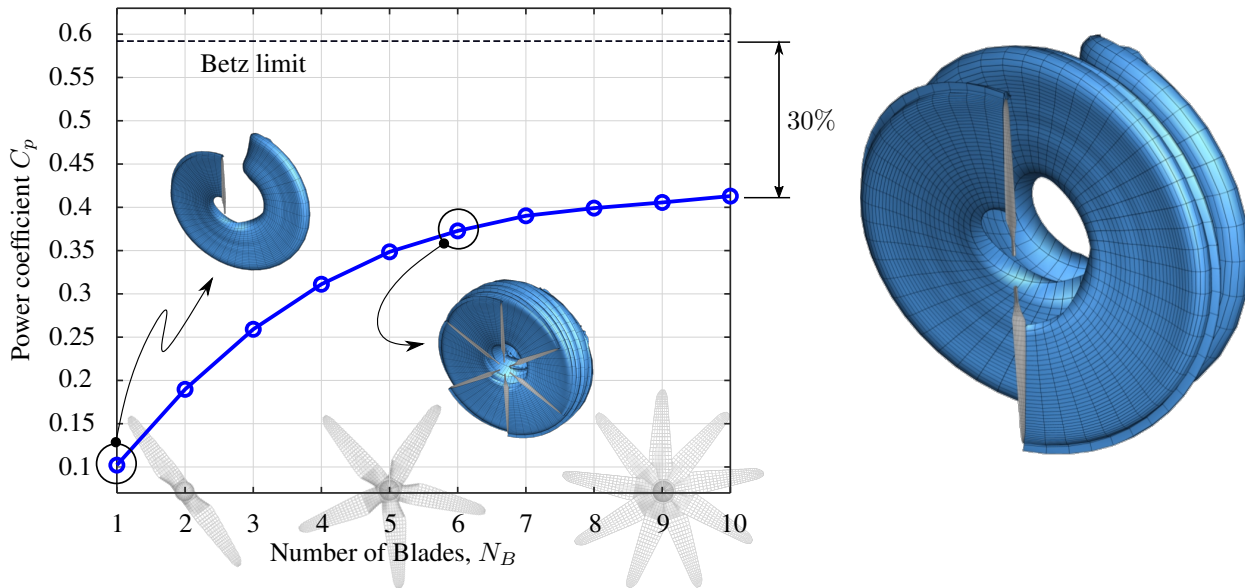


Figure 15. power coefficient as a function of the rotor solidity.

established wind turbine concepts such as: the Sandia 100-meter 13.2MW wind turbine SNL100-00 and the DTU 10 MW reference wind turbine. Finally, we show the versatility and potential of the mesher through the generation of two different entire wind farms. Additionally, without falling into quantitative aspects about the aerodynamic loads generated on the blades, we present some qualitative snapshots of the wakes emanating from the wind park by using the method described in Section 4.

All study cases presented in this work, the `VLMSim` solver was run on a desktop computer with an Intel(R) Core(TM) i7-8700 CPU at 3.20GHz with 16 GB of RAM memory.

5.1 Solidity study

The rotor solidity is a dimensionless number commonly used for designing rotors, such as: rotorcraft, propellers, and wind turbines. This is function of the aspect ratio and number of blades in the rotor thus providing a measure of how close a lifting rotor system is to an ideal actuator disk in momentum theory. Rotor solidity σ is defined as the fraction of the annular area in the control volume which is covered by the blades, i.e.,

$$\sigma(r) = \frac{c(r)N_B}{2\pi r}, \quad (26)$$

where $c(r)$ is the local chord and r is the radial position of the annular control area.

To analyze the influence of rotor solidity on the power output of a wind turbine, we consider ten different configurations, where the number of blades is varied from 1 to 10. We select a blade similar to the SNL100-00 wind turbine. The rest of the parameters are as follows: air density $\rho = 1.29 \text{ kg/m}^3$, free-stream velocity $V_\infty = 13.0 \text{ m/s}$, wind turbine radius $R = 110 \text{ m}$,



angular velocity $\Omega_r = 7.44$ RPM, and rotor swept area $A_r = \pi R^2$. As a reference power, we select the wind power crossing
 615 the rotor area, i.e.,

$$P_{\text{ref}} = \frac{1}{2} \rho V_{\infty}^3 A_r. \quad (27)$$

which allows us to introduce the power coefficient as $C_p = P/P_{\text{ref}}$. Fig. 15 depicts the C_p as a function of the number
 of blades. VLMSim predicts a solution that is in complete agreement with theoretical results. The study shows that power
 coefficient increases rapidly at first with the number of blades. Although the power continues to grow, the curve presents a
 620 very noticeable asymptotic behavior for 10 blades. Such a trend exhibit a difference of approximately 30% with respect the
 well-known Betz limit for 10 blades. Let's remember that it establishes a theoretical limit for the power that can be extracted
 from the wind ($C_p = 16/27 \approx 0.5926$), so that such difference of around 30% can be associated with a number of factors, such
 as: finite number of blades, blade geometry, non-optimal rotor configuration, etc. In practice real wind rotors have maximum
 C_p values in the range of 25% – 45% Bedon et al. (2012).

625 5.2 Yaw study

Another key factor associated with the power extraction from the wind is the yaw angle of the wind turbine with respect to the
 free-stream velocity. Rotor yaw reduces the effective projected area exposed to wind flow, thus reducing the energy conversion
 efficiency of the turbine. Yaw occurs when the wind direction is not perpendicular to the rotor plane. As consequence, the blade
 will experience a varying relative velocity and angle of attack, leading to even more unsteady aerodynamics phenomena.

630 It is clear that the effective velocity of the wind to be considered to estimated the output power of a yawed rotor is its
 projection on the rotor axis (see Fig. 16) Gebhardt (2012), which can be expressed as,

$$V_{\infty,e} = V_{\infty} \cos \gamma \cos \theta_y. \quad (28)$$

where the tilt angle γ was previously introduced, and θ_y is the yaw angle measured in a plane normal to the vertical (see Fig.
 16). In addition, the output power of a wind turbine can be expressed as a function of the aerodynamic torque and the rotor
 635 angular velocity as follows,

$$P = \mathbf{M} \cdot \boldsymbol{\Omega} = q_E L_C^3 C_M \Omega, \quad (29)$$

where $q_E = \frac{1}{2} \rho V_{\infty,e}^2$ is the effective dynamic pressure, L_C is some characteristic length (e.g., L_C in Table 6), C_M is aerody-
 namic moment coefficient, and Ω the rotor angular velocity. Introducing (28) into (29) and dividing by the power at $\theta_y = 0^\circ$,
 we get the following expression for a normalized output power,

$$640 \frac{P}{P_0} = \frac{C_M(\xi)}{C_M(0)} \cos^2 \theta_y, \quad (30)$$

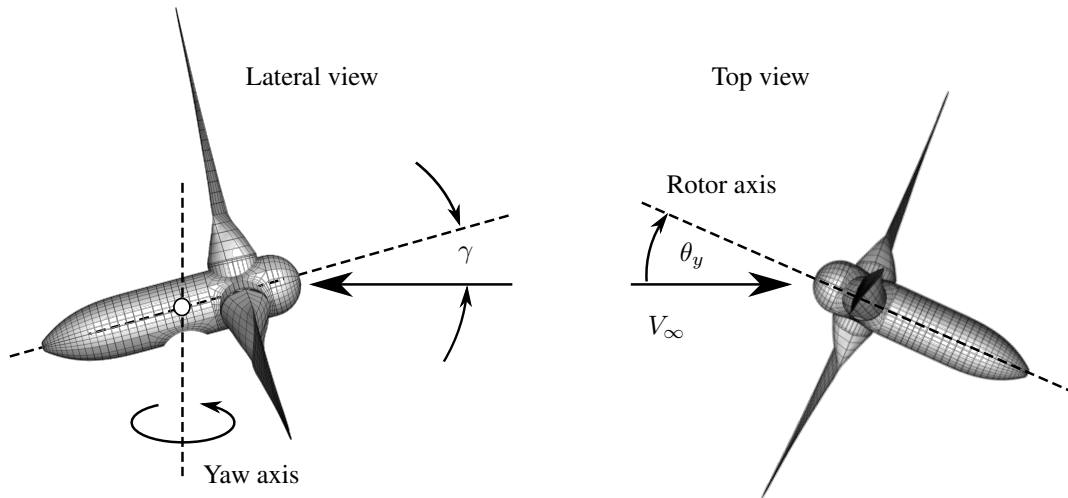


Figure 16. Free-stream direction.

where the ratio $C_M(\xi)/C_M(0)$ is a nonlinear function of θ_y . However, it approaches unity for small values of yaw angle. Therefore, as a first approximation, it can be considered that the ratio P/P_0 behaves like the function $\cos^2\theta_y$.

To analyze the influence of yawed rotors on the power output of a wind turbine, we consider different values of θ_y ranging from -60° to 60° . For this study, we selected the SNL100-00 wind turbine operating under the same working conditions as in Subsection 5.1. The resulting output power is then normalized with respect to the power at $\theta_y = 0^\circ$.

In Fig. 17 we show how the yaw angle affects the normalized output power. For angles lower than 15° , the power practically behaves as the function $\cos^2\theta_y$, i.e., nonlinearities associated with $C_M(\theta_y)$ are small. Beyond 15° , simulations diverge significantly from the function $\cos^2\theta_y$, thus meaning that nonlinearities become important.

5.3 Pitch study

One of the main control parameters in wind turbines is the pitch angle θ_p , which allows to regulate the output power according to the environmental conditions. For flow velocities less than the rated wind speed, the blade pitch is modified in order to maximize the output power. Similarly, for flow velocities beyond the rated wind speed, the blade pitch is also modified in order to avoid excessive angular speeds or runaway events.

The pitch angle is defined as an inward rotation of the blade leading edge towards the center of rotation of the turbine; in other words, θ_p is the angle between the tip chord and the rotor plane (see Fig. 18). Moreover, the local pitch is usually expressed as a combination of the pitch angle and the twist angle, i.e., $\varphi(z) = \theta_p + \theta^s(z)$. It should be stressed that $\mathbf{V}_{\text{total}}$ is the actual wind velocity hitting a blade section located at a distance z from the blade root.

To analyze the influence of the pitch angle on the output power produced for a wind turbine, we carried out a series of simulations considering the same rotor configuration as before and a pitch angle ranging from -6° to 12° . Fig. 19 shows how

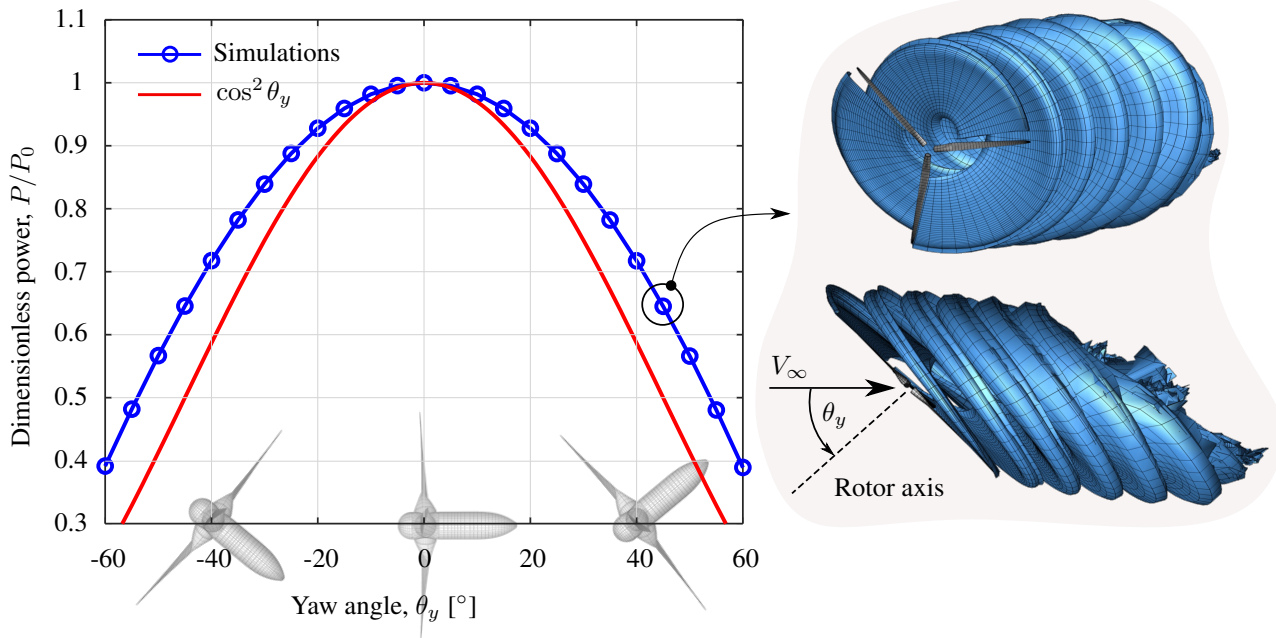


Figure 17. Normalized power as a function of the yaw angle.

660 the output power change as a function of the pitch angle. Note that the power is normalized with respect to the maximum power, $\bar{P} = P(\varphi_p)/P_{\text{ref}}$.

As it can be observed, the power curve is shifted to the right reaching its maximum at $\theta_p = 4^\circ$. For this case, a positive pitch angle is needed to get the maximum possible power. As expected, the pitch angle has a significant influence on output power, giving a glimpse of the great controllability associated with this parameter.

665 5.4 Pre-bend and cone angle study

Besides the twist and distribution of airfoils along the blade, cone angle and blade pre-bend are other two important parameters defining the geometry of a wind turbine rotor. The cone angle β is defined as the angle between the rotor plane and the blade longitudinal axis (see Fig. 20). Its main function is to tilt the rotor so that the blades are no longer at right angles to the nacelle, thus preventing them from hitting the tower as the rotor turns in strong winds Hau and von Renouard (2003).

670 Pre-bending was also primarily conceived to achieve tower clearance, i.e., to make sure that there is sufficient distance between the blade tips and the tower during the wind turbine operation (see Fig. 20). Both methods, coned rotors and pre-bending, require adjustments to the nacelle design.

Here we study how the cone angle and blade pre-bend affect power output independently of each other. To this end, we consider the following two different scenarios: *i*) no blade pre-bend and a cone angle ranging from -12° to 12° ; and *ii*) a blade
 675 pre-bend characterized by a blade tip deflection ranging from -20% to 20% and a cone angle $\beta = 0^\circ$. For all cases, the pitch

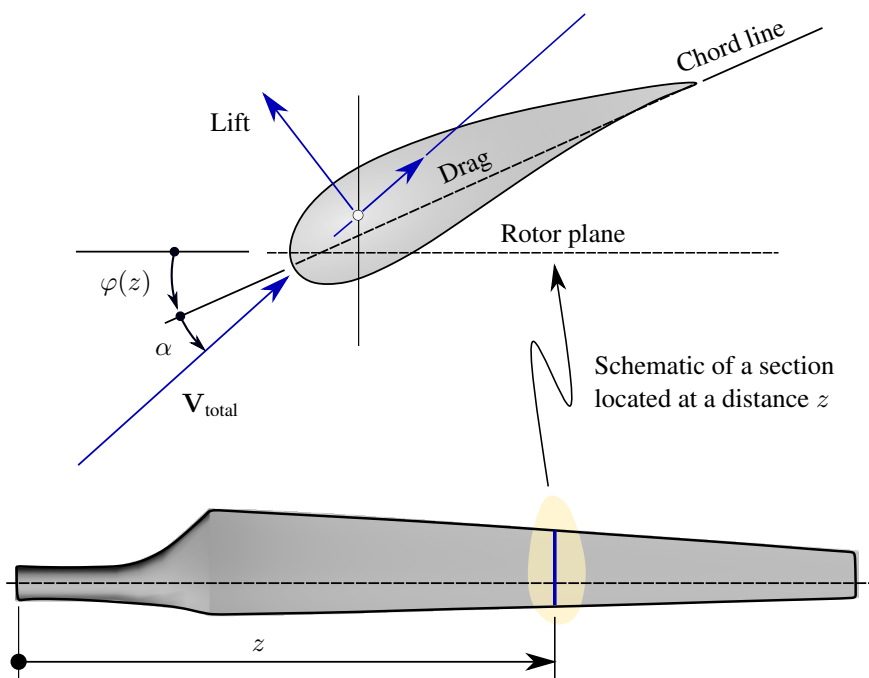


Figure 18. Definition of the pitch angle.

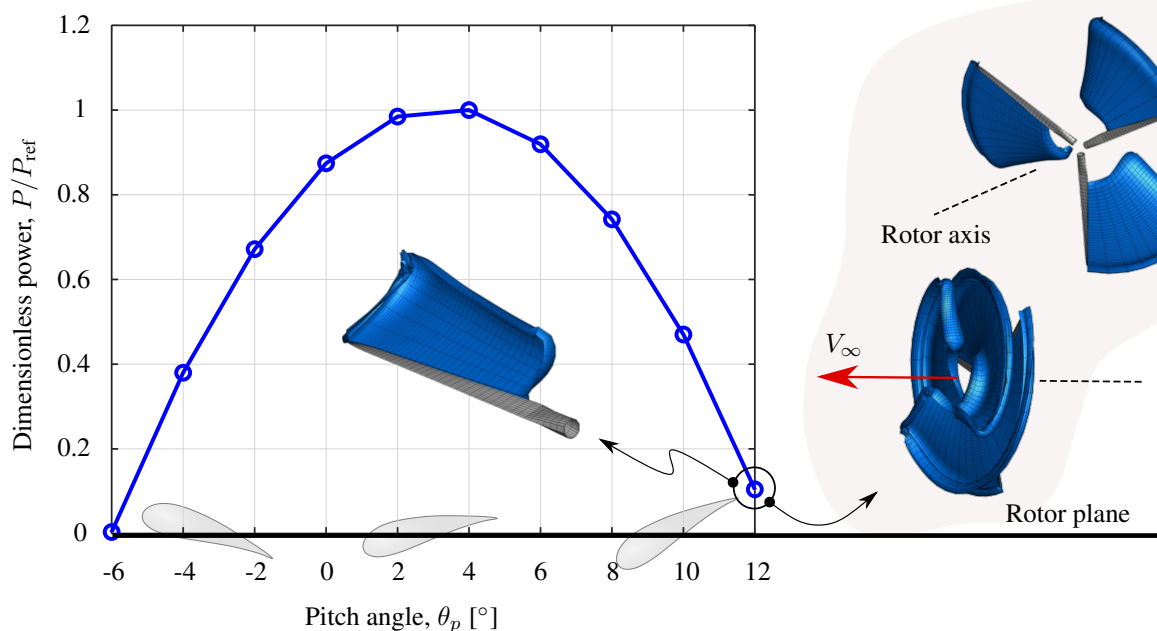


Figure 19. Normalized power as a function of the pitch angle.

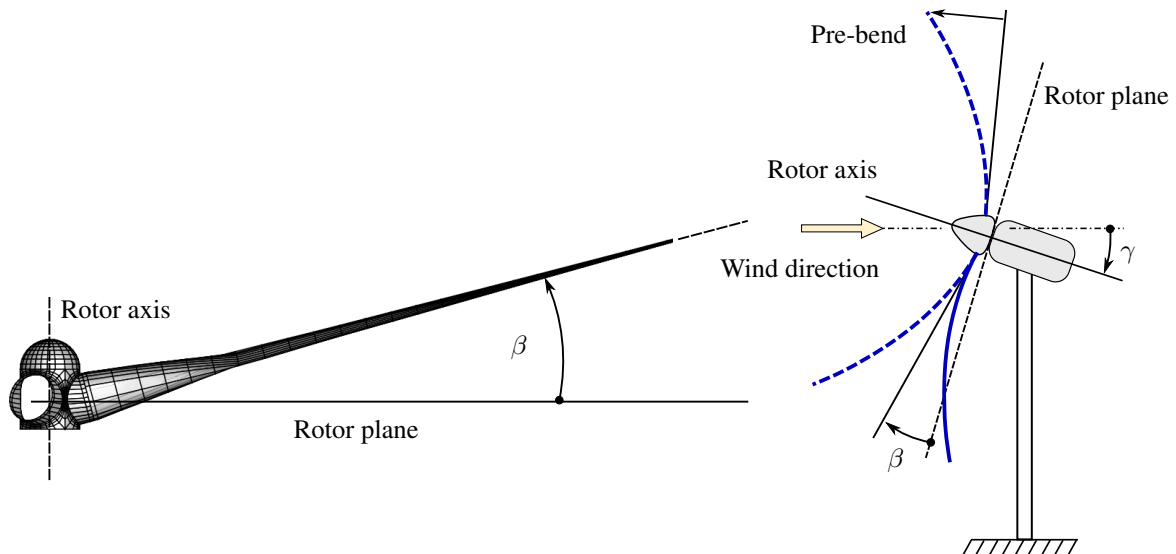


Figure 20. Definition of the cone angle and blade pre-bend.

angle is set to zero, $\theta_p = 0^\circ$. Here, pre-bending is included by using Zuteck’s procedure, already described in Section 2.2.4, and available in UVLMeshGen. The parameters of the Zuteck formula are listed in Table 7.

Table 7. Zuteck’s formula parameters

Variable	Value
ξ_1	1.6
x_{tip}	from -21.2 m to 21.2 m
z_0	0.0 m
N_{Gauss}	5 quadrature points
Δz	0.1
F_{bend}	option 2

The reader can find an explanation of such parameters in Appendix A, Table A.5. Both tip deflection x_1 and cone angle range were calculated with the goal of having a tip blade deflection of 20% of the rotor radius (i.e., blade length + hub radius, that is 106 m). For this study we selected again the SNL100-00 wind turbine operating under the same working conditions as in the previous subsections. For this study, the power is normalized with respect to the power obtained for the reference configuration, which is characterized by no pre-bending and cone angle $\beta = 0^\circ$.

Fig. 21 shows that blade pre-bending or cone angles affect the power output in a similar way. As it can be observed, the power curves are both shifted to the left reaching their maximum at $\beta = -6^\circ$ and $x_1 = -6.9756$ m. These findings suggest that those rotors having downwardly inclined blades provide higher performance than those with positive cone angles or positive blade pre-bending. However, such sort of rotors are of no practical importance since in general cone angles and pre-bending

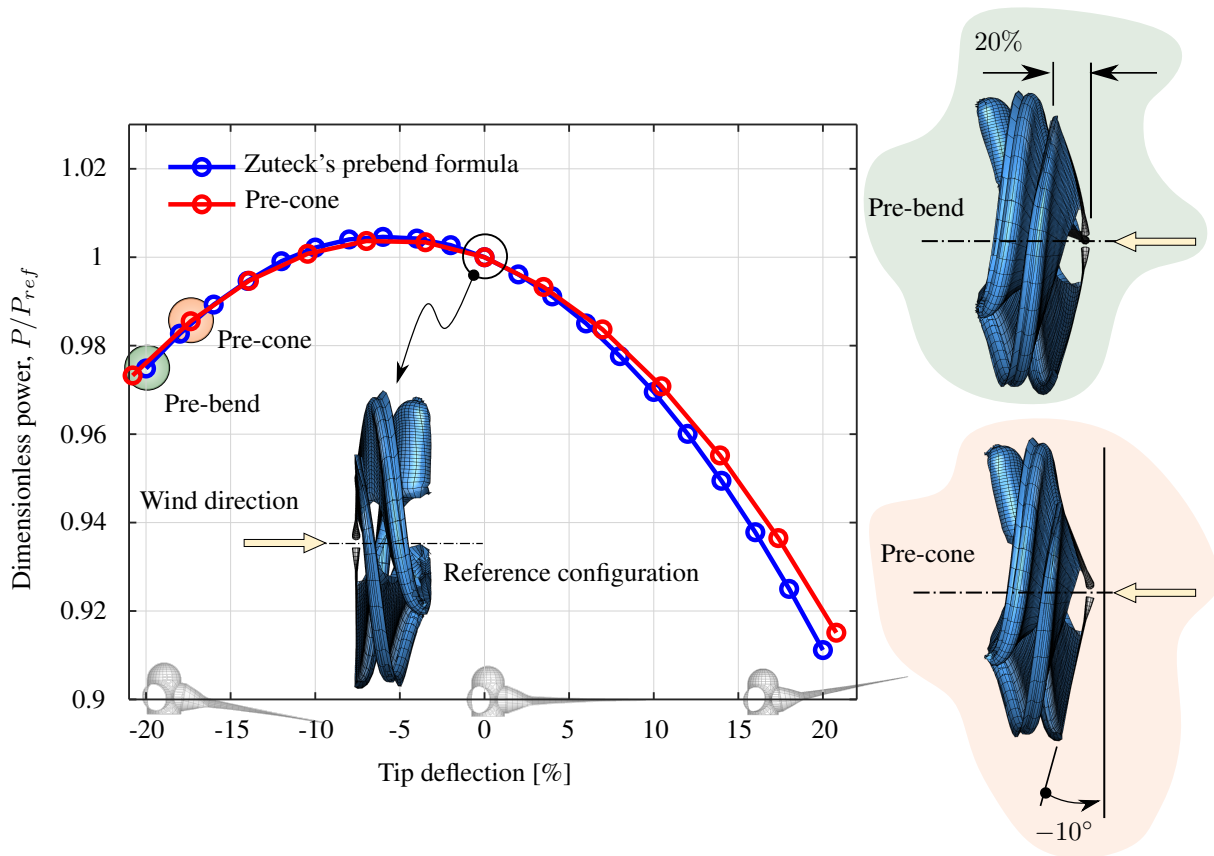


Figure 21. Normalized power as a function of pre-bending and cone angle.

are positives in order to achieve tower clearance. Although the results obtained in this study are original, they are only valid for the wind turbine considered here since there is not enough information available to draw general conclusions.

5.5 Aerodynamics of full wind turbines

690 In this subsection, we present some aerodynamic simulations of two well-known wind turbine concepts. One of them is the DTU 10 MW reference wind turbine developed by DTU Vindenergi (Institut for Vindenergi) Bak et al. (2013). The second turbine considered here is the SNL100-00 13.2 MW wind turbine concept developed by Sandia National Laboratories Griffith and Ashwill (2011).

695 According to the technical report Bak et al. (2013), the DTU 10 MW wind turbine was designed for offshore siting for an IEC class 1A wind climate, which is characterized by a rated wind speed of 11.4 m/s, minimum rotor speed of $\Omega_{min} = 6.0$ RPM, and maximum rotor speed of $\Omega_{max} = 9.6$ RPM. In addition, the DTU 10 MW blades have pre-bend in order to guarantee tower clearance. In Table 8 we list the main geometric and kinematic parameters used to compute the power and wake evolution of the DTU 10 MW wind turbine. A complete geometric description of the wind turbine is available in Bak et al. (2013). Moreover,



the reader can obtain the configuration files for generating the aerodynamic grid and kinematics for this study case in our
700 UVLMeshGen Github repository Roccia (2023).

Table 8. DTU 10 MW wind turbine - geometric and kinematic parameters

Variable	Value
Pitch angle, θ_p	7.266°
Rotor diameter	180.73 m
Pre-bend	deactivated ($F_{bend} = 0$)
Angular velocity, Ω	9.6 RPM
Free-stream velocity, V_∞	13.0 m/s
Characteristic velocity, V_C	13.0 m/s
Characteristic length, L_C	0.8376 m
Fluid density, ρ	1.225 kg/m ³
Number of time steps, $N_{\Delta t}$	668
Number of panels, N_{pb}	5176

In Fig. 22 we present an aerodynamic simulation of the DTU 10 MW wind turbine obtained by using the VLMSim flow
solver. The working parameters correspond to those specified in Table 8. Peaks down in the power curve arise as consequence
of the blades passing through the tower shadow. According to the simulation parameters, the period of each revolution is 6.316
s, thus giving three peaks per revolution. Such a result is in total agreement with the fact of having the passage of three blades
705 through the tower shadow per revolution.

Such a phenomenon is recognized as an aerodynamically unsteady region, where the flow angle and velocities are signif-
icantly affected. As the downwind turbine blades pass through this region of velocity deficit, the flow seen by the blade is
directly modified, thus resulting in periodical drops of the lift forces and, therefore, a power curve with peaks. Besides this
finding is justified from a physical point of view, its magnitude could be influenced by effects of numerical origin, for which
710 more studies are required to understand this phenomenon.

Another aspect worth mentioning is the interaction of the wakes with the tower. As can be seen in Fig. 22), it may seem
that the flow solver considers some sort of wake rupture as used by Gebhardt et al. Gebhardt et al. (2010). However, VLMSim
does not have such a capacity, but it can handle wake-body interference to some extent by using a vortex core-growth strategy
based on the Lamb-Ossen model (Bhagwat and Leishman (2002); Roccia et al. (September 2018)). This add-on allows for
715 diffusing vortex segment intensities to handle situations, in which two or more vortex segments are getting extremely close.
Despite the fact that both methods are radically different, they predict very similar behaviors in terms of the peaks observed
in the aerodynamic loads (consequence of the tower shadow). Furthermore, it should be emphasized that the in-house solver
VLMSim has been extensively verified and validated Verstraete et al. (2023).

The second wind turbine adopted here is the Sandia 13.2 MW SNL100-00 with a 100 meter blade length, which is based
720 on the NREL 5 MW model Jonkman et al. (2009). The cut-in, cut-out and rated wind speeds are 3.0 m/s, 25 m/s and 11.3
m/s, respectively. The maximum rotation rate of this variable speed machine is $\Omega_{max} = 7.44$ RPM. In Table 9 we list the main
geometric and kinematic parameters used to compute the power and wake evolution of this wind turbine. Moreover, the reader

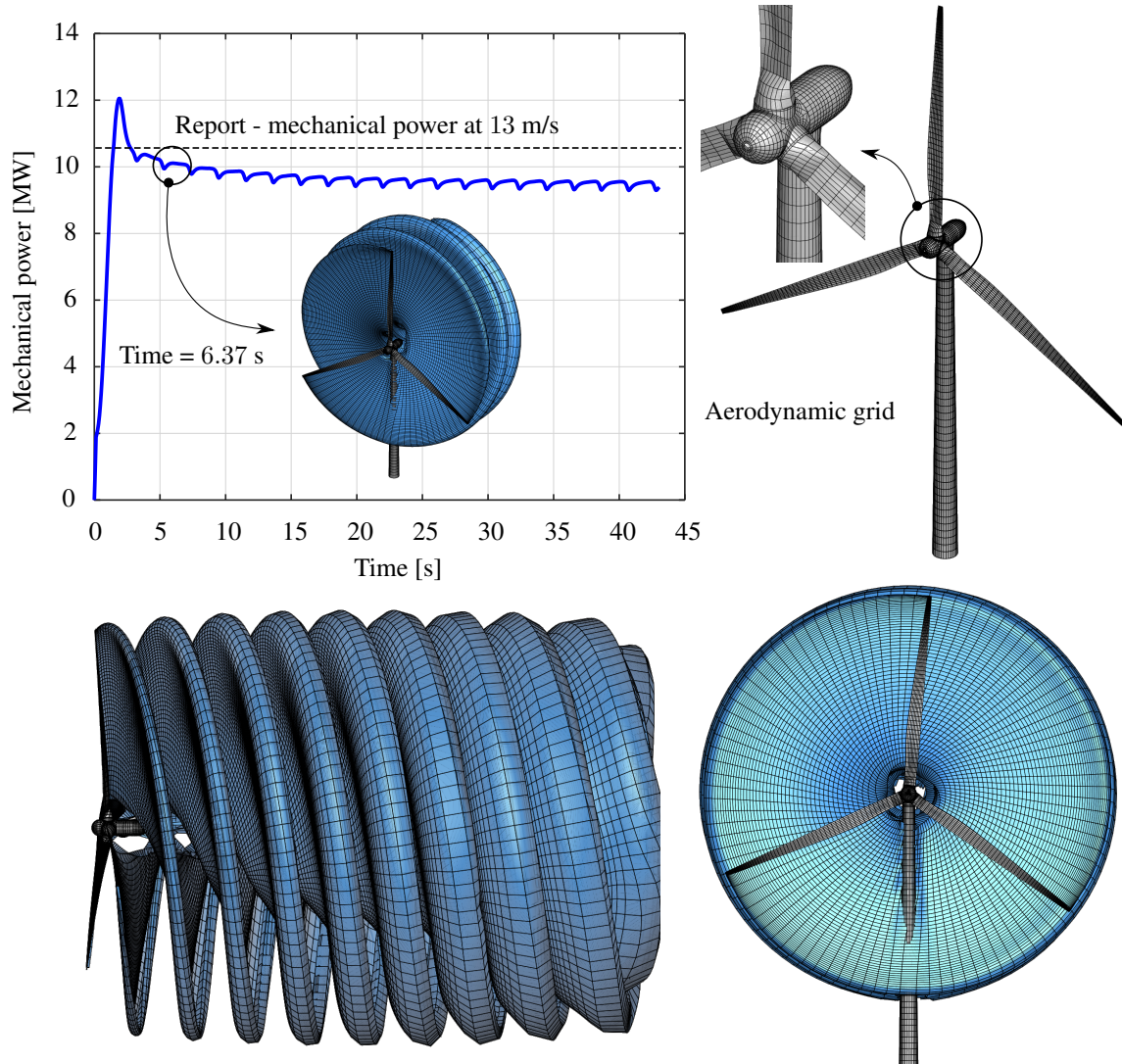


Figure 22. Aerodynamic simulation of the DTU 10 MW wind turbine.

can obtain the configuration files for generating the aerodynamic grid and kinematics for this study case in our UVLMeshGen Github repository Roccia (2023).

725 In Fig. 23 we present the time-series of the output power for the SNL100-00 wind turbine together with the spatial evolution
of the wake. The power after 40 s of simulation is around 12.4 MW (steady state), this value being 6% less than the theoretical
power predicted in the technical report. This difference may be attributed to different sources. First of all, we are considering
a constant pitch angle throughout the simulation, when in fact this machine operates with a variable pitch angle. Second, the
report utilizes a version of the low-fidelity and well-known blade element momentum theory to predict the aerodynamic forces,
730 which can lead to some differences when compared to more accurate methods such as mid-fidelity vortex-based approaches.



Table 9. Sandia 13.2 MW SNL100-00 - geometric and kinematic parameters

Variable	Value
Pitch angle, θ_p	3.5°
Rotor diameter	208 m
Angular velocity, Ω	7.0 RPM
Free-stream velocity, V_∞	13.0 m/s
Characteristic velocity, V_C	13.0 m/s
Characteristic length, L_C	1.1252 m
Fluid density, ρ	1.225 kg/m ³
Number of time steps, $N_{\Delta t}$	500
Number of panels, N_{pb}	4596

However, the results included here are not aimed at an exhaustive aerodynamic study of the aerodynamic performance of turbines, but to show the capacity of the UVLMeshGen to generate suitable UVLM meshes in a fast and versatile way.

Finally, the peaks observed in the power curve have the same origin as those discussed above for the DTU 10 MW wind turbine, however their magnitudes are slightly larger. As previously stated, although the appearance of these peaks has a well-
 735 founded physical explanation, their magnitude may not be entirely correct, and may be affected by numerical issues.

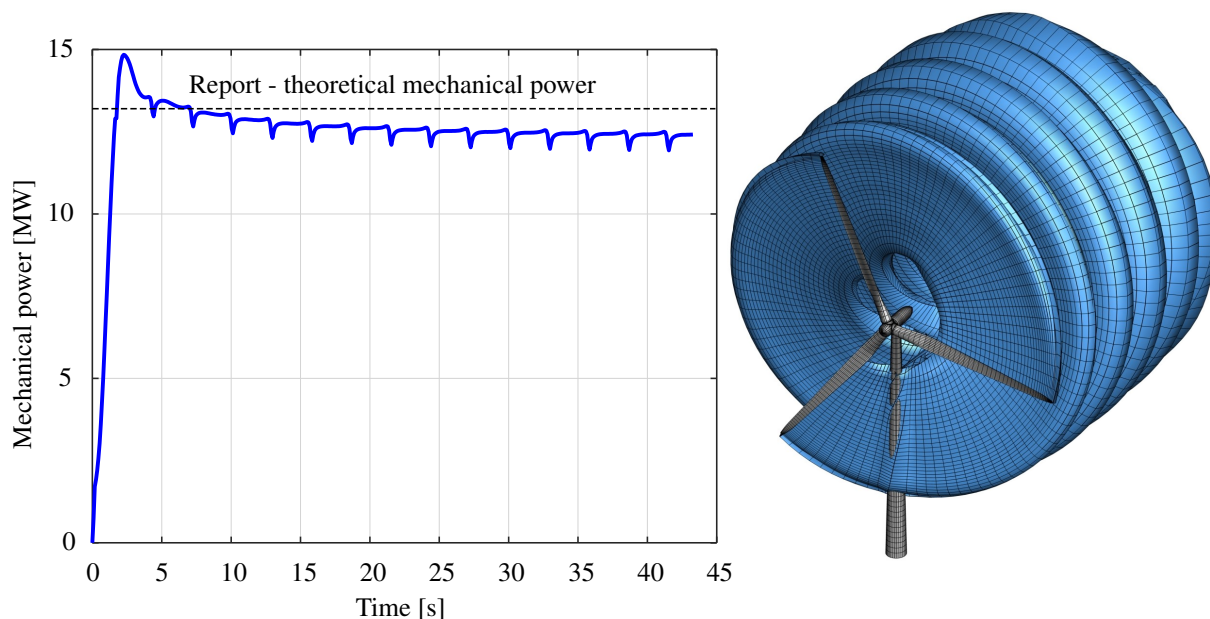


Figure 23. Aerodynamic simulation of the Sandia 13.2 MW SNL100-00 MW wind turbine.



5.6 Wind energy farms

This subsection has a main goal to show the versatility and capacity of the meshing tool developed through the generation of two hypothetical wind farms. These examples give a glimpse the scalability power of the UVLMeshGen in generating aerodynamic grids of heterogeneous parks consisting of an arbitrary number of wind turbines, including the terrain modeling
740 (for both onshore and offshore farms). The meshes obtained from UVLMeshGen are used as input for the VLMSim solver to carry out qualitative aerodynamic simulations of such wind farms.

5.6.1 Onshore wind farm

Here we focus on modeling an onshore wind farm consisting of four wind turbines, of which two turbines are of the DTU 10 MW type and the other two are of the SNL100-00 type. Fig. 24 shows the layout of the park including and Table 10 lists the
745 main geometric and kinematic parameters used to carry out an aerodynamic simulation of the entire wind farm.

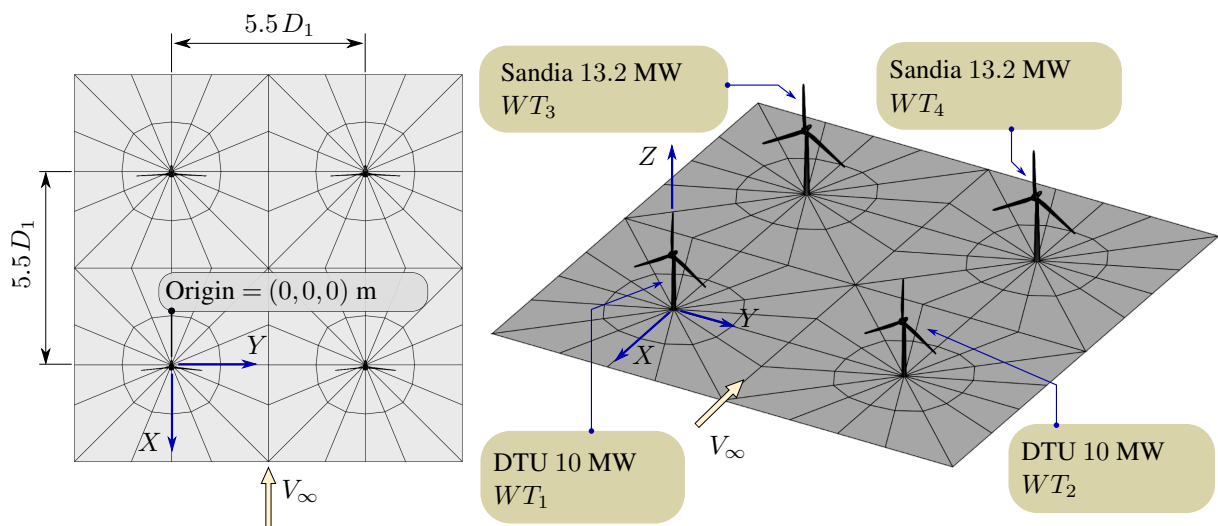


Figure 24. Onshore wind farm layout.

As can be seen from the schematic, the grid used is relatively coarse in order to reduce the computational cost associated with the aerodynamic simulation. In UVLM-based solvers there are mainly two time-consuming processes, namely: *i*) the computation of the circulations which requires solving a linear system of dimension $N_{pb} \times N_{pb}$; and *ii*) the convection of the wakes. Although for systems discretized into a large number of panels the solution of the linear system may take longer
750 initially, as time evolves, the wake convection undoubtedly becomes the bottleneck of the aerodynamic simulation.

Fig. 25 shows the aerodynamic simulation for the entire onshore wind farm after 100 time steps. Clearly, the wakes emanating from the DTU wind turbine develop more than those shed from the Sandia machine because of the different angular velocities. However, the time step used for the whole farm is the same and its value is determined according to what is explained in the



Table 10. Onshore wind farm - geometric and kinematic parameters

Variable	Value
Free-stream velocity, V_∞	13.0 m/s
Fluid density, ρ	1.225 kg/m ³
DTU WT Angular velocity, Ω_1	9.6 RPM
Sandia WT Angular velocity, Ω_2	7.0 RPM
DTU rotor diameter, D_1	180.73 m
Sandia rotor diameter, D_2	208 m
Number of time steps, $N_{\Delta t}$	100
Number of panels, N_{pb}	7336

Subsection 3.5. As an example and to bring up the computational cost of simulating wind turbine farms, the simulation time
 755 for 100 time steps of the farm described above took 28 hs on the desktop computer described at the beginning of this section.

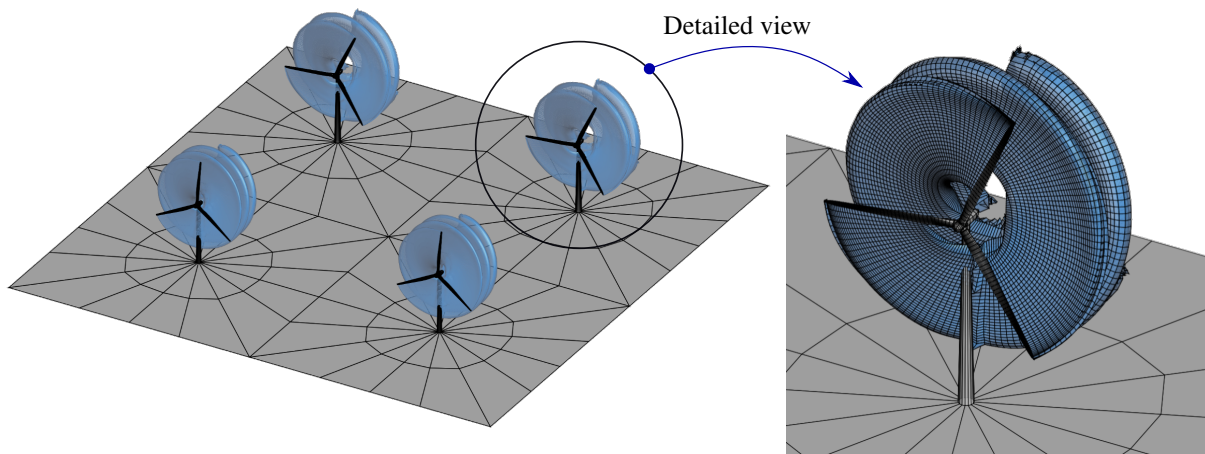


Figure 25. Aerodynamic simulation of an onshore wind farm composed of four wind turbines.

5.6.2 Offshore wind farm

Finally, we present the modeling of an offshore wind farm consisting of nine IEA 15 MW wind turbines. This reference wind turbine is a Class IB direct-drive machine, with a rotor of 240 m and a fixed-bottom monopile support structure which was jointly developed between the National Renewable Energy Laboratory and the Technical University of Denmark Gaertner et al.
 760 (2020). The terrain was modeled with a sinusoidal function to simulate an ocean wave profile, similar to the example shown in Fig. 13, to incorporate sea level as a boundary for the flow solver. Although this wave does not have movement (or kinematics), it is not the objective of this work to carry out an exhaustive study of offshore farms, but rather to show the versatility of the meshing tool. Fig. 26 shows the layout of the park including and Table 11 lists the main geometric and kinematic parameters used to carry out an aerodynamic simulation of the entire wind farm.

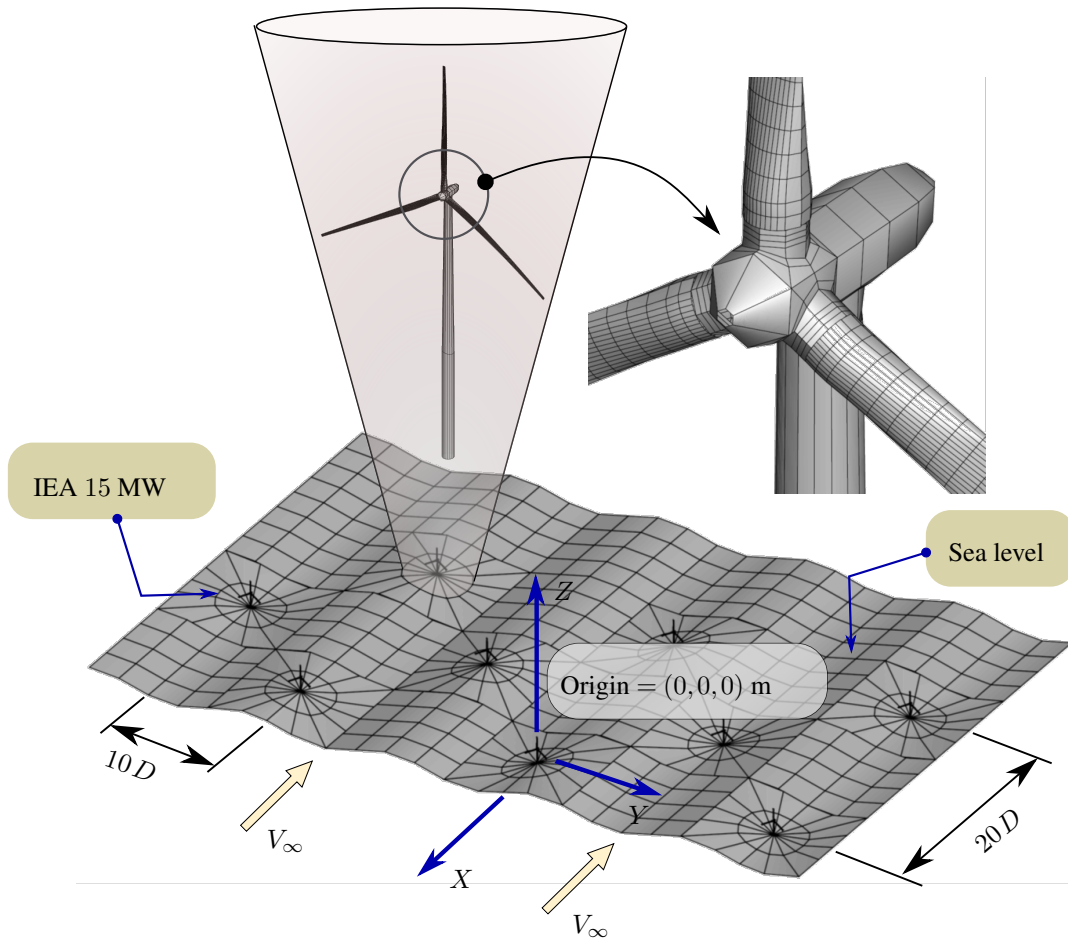


Figure 26. Offshore wind farm layout.

765 Fig. 27 shows the aerodynamic simulation for the entire offshore wind farm after 200 time steps. As before, the grid used
for this farm is coarse in order to reduce the computational cost associated with the aerodynamic simulation. Even with a
coarse mesh, the total number of panels is around 35000, which translates into an aerodynamic matrix of the order of 1×10^9
elements. The solution of the linear system plus wake convection has increased the computational cost for this example from
28 hs (onshore farm) to 96 hs.

770 Although the aerodynamic simulations of wind turbine farms presented above are purely qualitative in nature, they do
highlight the time-consuming problem associated with these types of studies. Although these cases have been run on a relatively
outdated desktop computer, it is necessary to implement methods to speed up UVLM-based solvers. On this basis, it is essential
to explore the use of the fast multipole technique in order to reduce from $O(n^2)$ to $O(n)$ and $O(n \log n)$ the number of
operations performed by the Biot-savart law Bogateanu et al. (2010), or the implementation of parallelization and vectorization
775 algorithms in graphics processing units (GPU) using CUDA for example.



Table 11. Offshore wind farm - geometric and kinematic parameters

Variable	Value
Free-stream velocity, V_∞	13.0 m/s
Fluid density, ρ	1.225 kg/m ³
IEA WT Angular velocity, Ω	9.6 RPM
Rotor diameter, D	246 m
Number of time steps, $N_{\Delta t}$	200
Number of panels, N_{pb}	35178

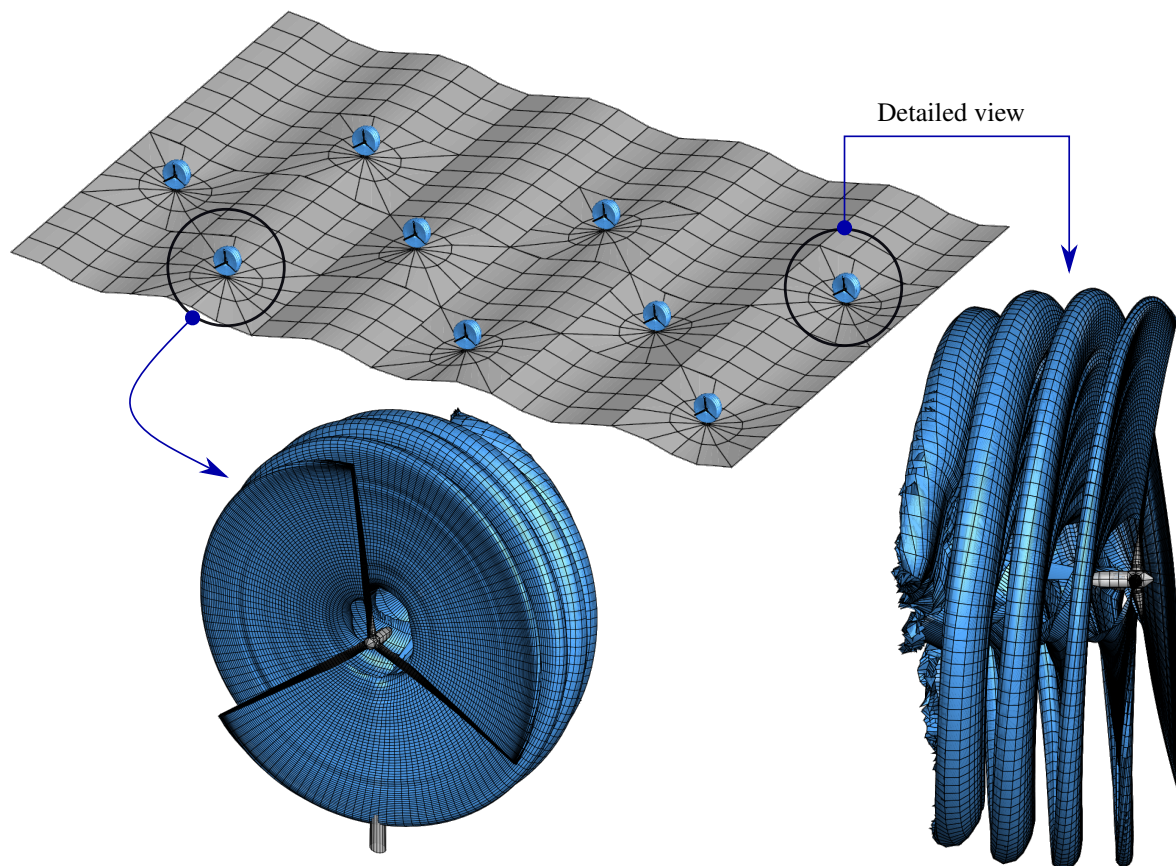


Figure 27. Aerodynamic simulation of a offshore wind farm composed of nine wind turbines.

6 Conclusions

In this article, we presented a detailed description of the geometric modeling and computational implementation of an interactive and versatile UVLM-oriented mesh generator for wind turbines and onshore/offshore wind farms. The meshing tool was developed entirely in Matlab[®] and is easily adaptable to GNU OCTAVE. We also provided a full explanation of the



780 input data needed by the tool, including tables where the reader can find a description of all the variables and their names in
Matlab® . The output data provided by UVLMeshGen, nodal coordinates and connectivity arrays, were successfully used by
the UVLM-based solver VLMSim. In addition, the meshing tool was robust when generating different configurations of WTs
and WFs according to: airfoils data, geometric parameters, terrain topography, wind farm layouts, and meshing requirements.
UVLMeshGen has been tested with a large number of examples and has proven to be efficient in building aerodynamic grids of
785 onshore/offshore wind turbines and wind farms. Furthermore, UVLMeshGen was intensively used to generate all the meshes
for the aerodynamic simulations included in Section 5. Although such results were mainly conceived to show the capabilities of
the developed meshing tool, the versatility of the mesh generator allowed us to investigate different rotor configurations, whose
aerodynamic characteristics are not commonly found in the literature. Among these findings, pre-cone angle and pre-bending
were found to affect the output power in a similar way.

790 Although a freely available meshing tool such as UVLMeshGen may significantly contribute to the community focused on
wind farm aerodynamic simulations, it still has important limitations that should be addressed in the future as a follow-up to
this contribution. Among the most important improvements that can be made we identify: *i*) the meshing of different types
of substructures (for offshore wind energy); *ii*) the meshing of the blade considering its thickness; *iii*) the kinematics of the
substructure; and *iv*) the kinematics of the sea surface (to simulate waves). Finally, we encourage the community to actively
795 participate in this open project related to providing and improving meshing tools intended for potential flow solvers for the
wind energy sector.



Appendix A: Appendix

Table A.1. Tower variables

Variable	Structure field name	Description
R_{T1}	RConTTow	Tower top radius (tower-nacelle connection)
R_{T2}	RGroundTow	Radius of the tower at ground/sea level
N_{T1}	NZTow	Number of nodes along the Z -direction
N_{T2}	NCircTow	Number of nodes along the tangential direction

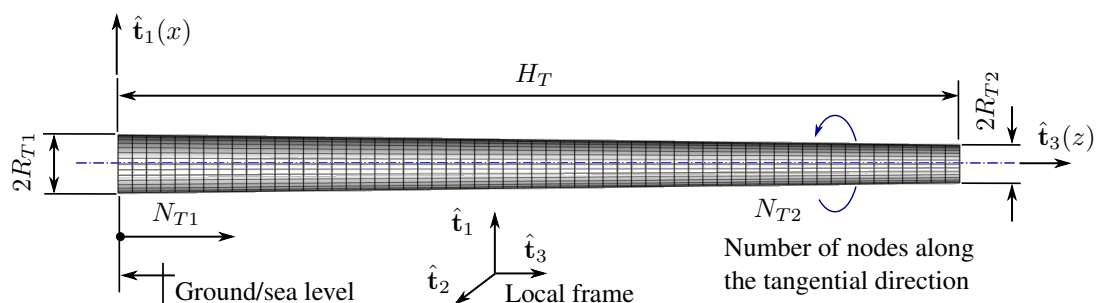




Table A.2. Monopile variables

Variable	Structure field name	Description
L_M	LMon	Monopile length
R_{M1}	RWaterMon	Monopile radius at sea level (tower-monopile)
R_{M2}	RDeepMon	Monopile radius at sea floor
N_{M1}	NZMon	Number of nodes along the Z -direction
N_{M2}	NCircMon	Number of nodes along the tangential direction

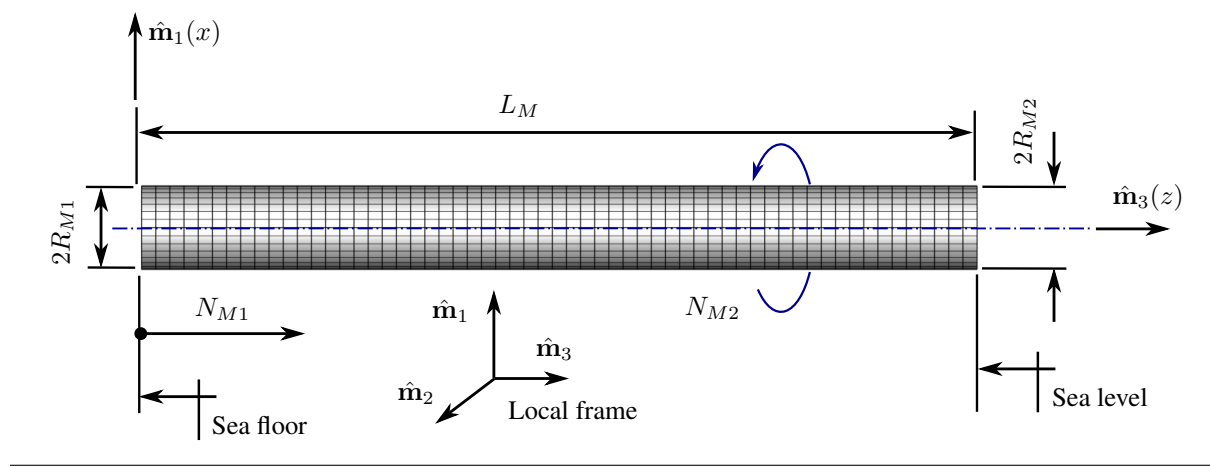




Table A.3. Nacelle variables

Variable	Structure field name	Description
R_{N1}	RadNac	Nacelle radius
R_{N2}	RTailNac	Nacelle tail radius
R_{N3}	RConTNac	Radius of the nacelle-tower connector piece
L_{N1}	LCylNac	Length of the cylindrical part of the nacelle
L_{N2}	LTailNac	Length of the nacelle tail
L_{N3}	LConTNac	Length of the nacelle-tower connector piece
N_{shape}	ShapeTailNac	Nacelle tail shape (options: {1, 2, 3, 4})
N_{N1}	NCircNac	Number of nodes along the tangential direction of $\mathcal{N}_{GO_1}^2$
N_{N2}	NRadNac	Number of nodes along the radial direction of $\mathcal{N}_{GO_1}^2$
N_{N3}	NCircCylNac	Number of nodes along the tangential direction of $\mathcal{N}_{GO_2}^3$
N_{N4}	NTailNac	Number of nodes along the tail x -direction
N_{N5}	NZCoupNac	Number of nodes along the Z -direction of $\mathcal{N}_{GO_2}^1$

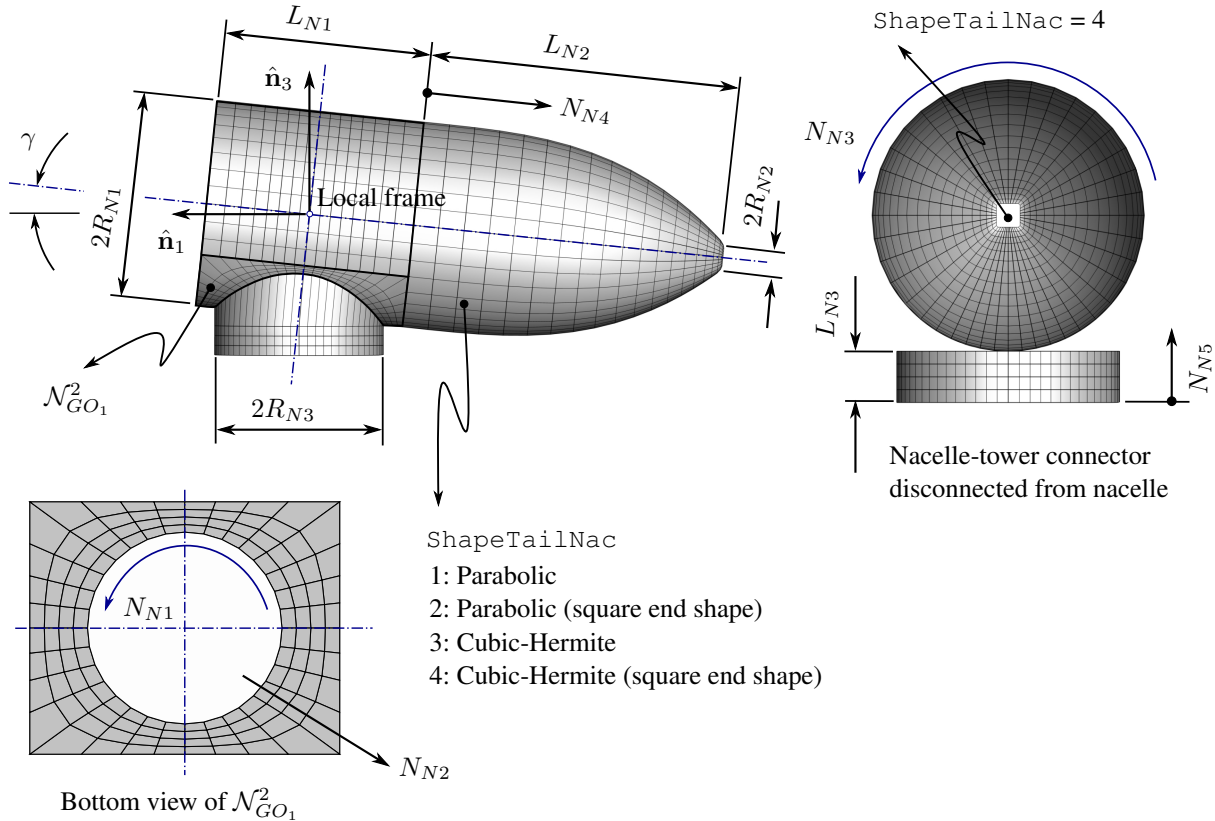




Table A.4. Hub variables

Variable	Structure field name	Description
R_{H3}	RBladeHub	Radius of the blade-hub connector piece
L_{H1}	LCylHub	Length of the cylindrical part of the hub
L_{H2}	LNoseHub	Length of the hub nose
δ_{hub}	TrimNoseHub	Trim percentage (1% to 10%) of the hub nose tip
H_{shape}	ShapeNosHub	Hub nose shape (options: {1, 2, 3})
N_{H1}	NCircHub	Number of nodes along the tangential direction of $\mathcal{N}_{GO_1}^k$
N_{H2}	NRadHub	Number of nodes along the radial direction of $\mathcal{H}_{GO_1}^k$
N_{H3}	NZcoupHub	Number of nodes along the longitudinal direction of $\mathcal{N}_{GO_2}^k$
N_{H4}	NNoseHub	Number of nodes along the nose x -direction

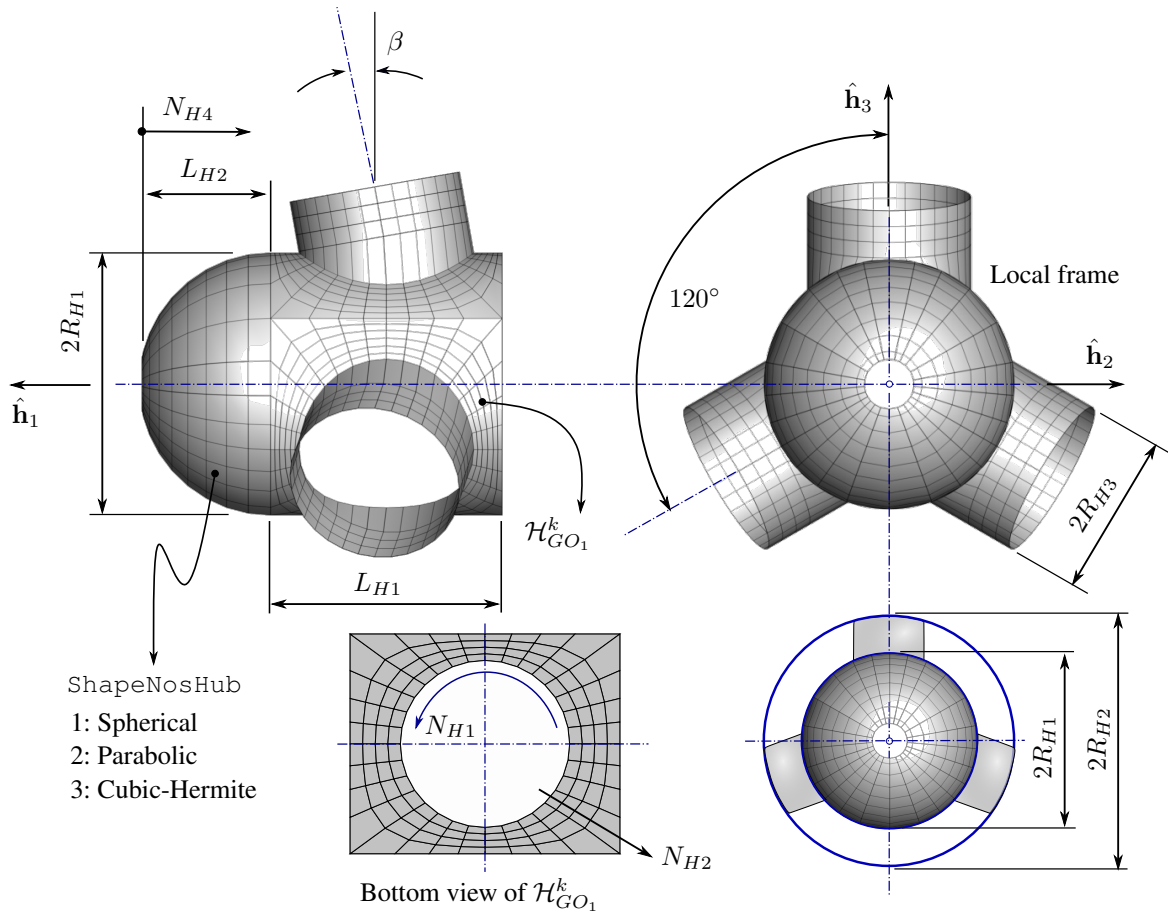




Table A.5. Blade variables

Variable	Structure field name	Description
*.DAT	NameBld	Input file containing the blade geometric description
L_B	LBld	Blade length (from root to tip)
$L_{B,LS}$	LSLBld	Lifting surface length
$L_{B,R}$	RLBld	Blade root length
N_{B1}	NBldC	Number of nodes along the blade chordwise direction
N_{B2}	NBldS	Number of nodes along the blade spanwise direction
F_{shed}	ShedBld	Shedding zones (options: {1, 2})
N_{gap}	GAPBld	Number of nodes in the ‘Gap’ zone
ξ_1	aBld	Exponent in Zuteck’s formula (pre-bend)
ξ_2	bBld	Exponent in Zuteck’s formula (sweep)
x_{tip}	r1Bld	Tip deflection in Zuteck’s formula (pre-bend)
y_{tip}	r2Bld	Tip deflection in Zuteck’s formula (sweep)
z_0	X0Bld	Blade starting point for sweep/pre-bend (0 to 1)
N_{Gauss}	QGaussBld	Gauss point number for the sanity analysis
Δz	DXBld	Increment for computing numerical derivatives
F_{bend}	Op1Bld	Pre-bend deformation (options: {0, 1, 2})
F_{sweep}	Op2Bld	Sweep deformation (options: {0, 1, 2})

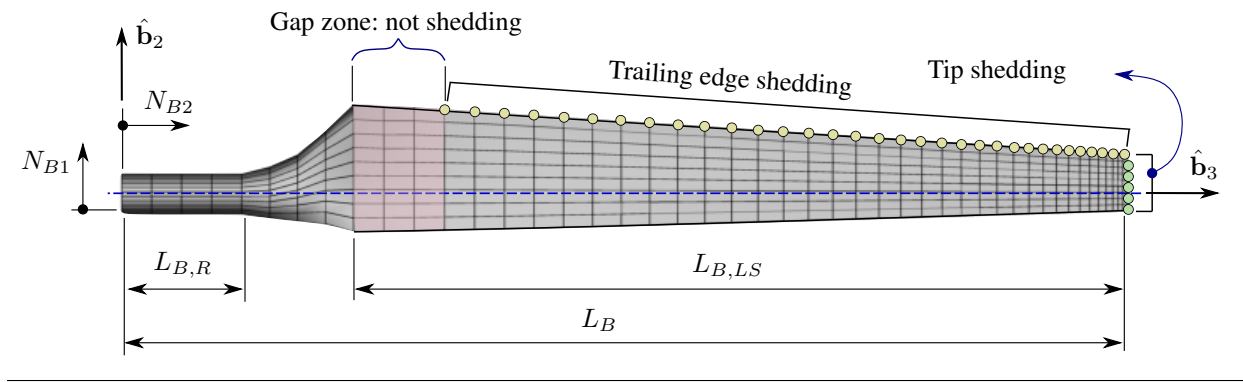
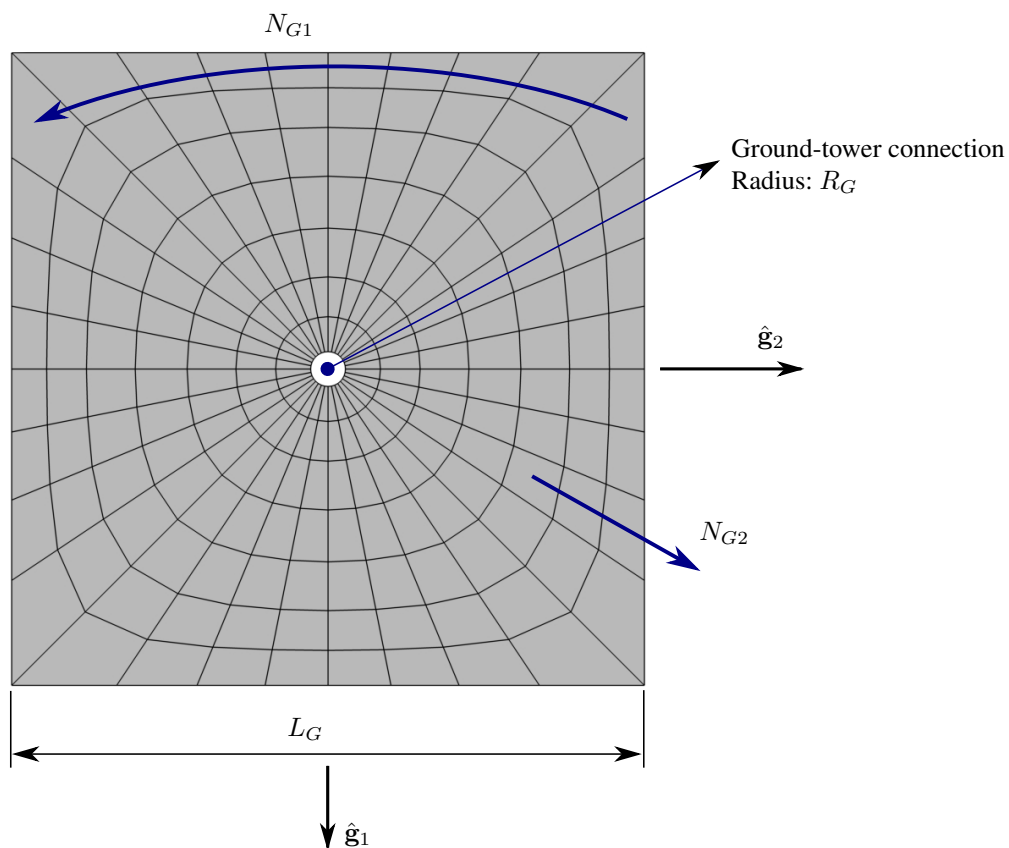




Table A.6. Ground variables

Variable	Structure field name	Description
R_G	RTowGround	Ground-tower connection radius
L_G	LGround	Side length of the square representing the ground area
N_{G1}	NCircGround	Number of nodes along the tangential direction of \mathcal{G}_{GO_1}
N_{G2}	NRadGround	Number of nodes along the radial direction of \mathcal{G}_{GO_1}





Appendix B: Appendix

Table B.1. WIND_TURBINE - main fields and substructure variables

Structure field name	Description
XYZTower	Coordinate array associated with the tower
NACPART	Structure field indexed by the number of components of the nacelle. Each index contains, as a sub-field, the nodal coordinates of each nacelle component
HUBPART	Structure field indexed by the number of components of the hub. Each index contains, as a sub-field, the nodal coordinates of each hub component
BLDPART	Structure field indexed by the number of components of the blade. Each index contains, as a sub-field, the nodal coordinates of each blade component
XYZMON	Coordinate array associated with the monopile
MPOINT	Coordinate of the intersection point between the rotation axis and the longitudinal axis of the tower with respect to a local wind turbine reference frame
MAxis	Rotation axis of the wind turbine

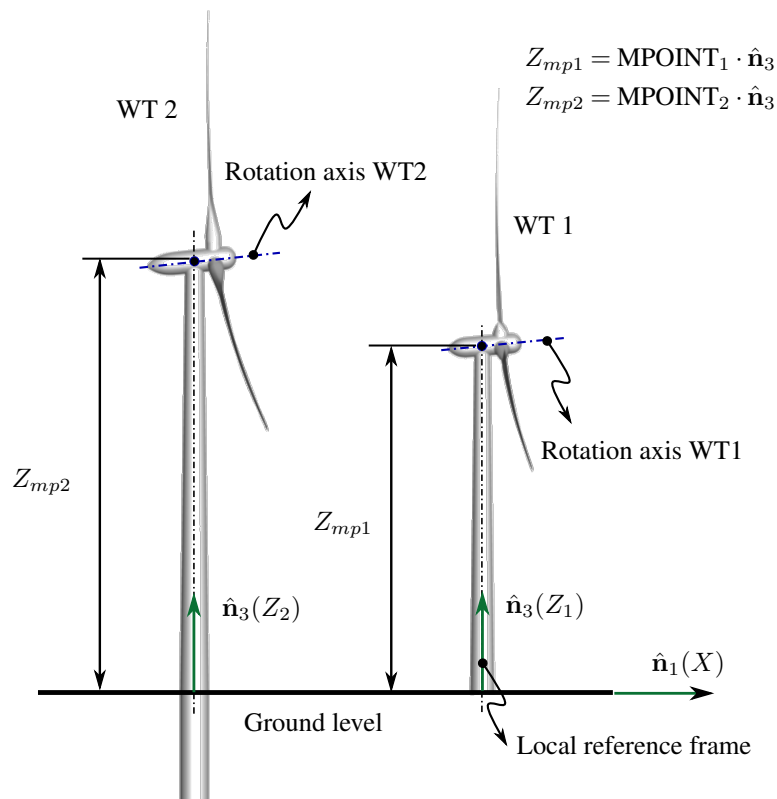




Table B.2. CONNECT - main fields and substructure variables

Structure field name	Description
TOWER	Tower connectivity array
NACPART	Structure field indexed by the number of components of the nacelle. Each index contains, as a sub-field, the connectivity array of each nacelle component
HUBPART	Structure field indexed by the number of components of the hub. Each index contains, as a sub-field, the connectivity array of each hub component
BLDPART	Structure field indexed by the number of components of the blade. Each index contains, as a sub-field, the connectivity array of each blade component
MONOPILE	Monopile connectivity array

Table B.3. GROUND_FARM - main fields and substructure variables

Structure field name	Description
NumBox	Number of patches (denoted also by N_{Gp})
IDWT	Array of dimension $1 \times N_{Gp}$. Each component represents a terrain patch. A null value means that such a patch does not contain any wind turbine inside it. A non-zero value means that that patch contains a wind turbine and the number refers to which wind turbine. Only one wind turbine is allowed to be allocated per patch
PATCH	Structure field indexed by the number of patches into which the terrain was divided. Each index contains, as a sub-field, nodal coordinates, CP coordinates, and connectivity array of each terrain patch



Table B.4. KINEMATICS (i) .WT - main fields and substructure variables

Structure field name	Description
XYZTower	Tower coordinate array
XYZCPTower	Tower CP coordinate array
XYZVCPTower	Tower CP velocity array
NACPART	Structure field indexed by the number of components of the nacelle. Each index contains, as a sub-field, nodal coordinates, CP coordinates, and CP velocities of each nacelle component
HUBPART	Structure field indexed by the number of components of the hub. Each index contains, as a sub-field, nodal coordinates, CP coordinates, and CP velocities of each hub component
BLDPART	Structure field indexed by the number of components of the blade. Each index contains, as a sub-field, nodal coordinates, CP coordinates, and CP velocities of each blade component
XYZMonopile	Monopile coordinate array
XYZCPMonopile	Monopile CP coordinate array
XYZVCPMonopile	Monopile CP velocity array
MPOINT	Monopile connectivity array
MAxis	Monopile connectivity array



Code and data availability. The UVLMeshGen source code and data sets are freely available under a Creative Commons Attribution 4.0 International License in <https://github.com/brunoroccia/UVLMeshGen-mesh-generator>.
800

Author contributions. Bruno Antonio Roccia: Conceptualization, Formal Analysis, Investigation, Methodology, Software, Writing - original draft, Writing - review & editing.

Luis Ramón Ceballos: Investigation, Software, Numerical simulations, Review & editing.

Marcos Leonardo Verstraete: Investigation, Software, Review & editing.

805 Cristian Guillermo Gebhardt: Conceptualization, Formal Analysis, Methodology, Software, Supervision, Writing - original draft, Writing - review & editing.

Competing interests. The authors declare that we have no known competing financial interests or personal relationships that could have appeared to influence the work reported in this manuscript.

Acknowledgements. C. Gebhardt gratefully acknowledges the support from the European Research Council via the ERC Consolidator Grant
810 “DATA-DRIVEN OFFSHORE” (Action No. 101083157).



References

- Abdelkefi, A., Ghommem, M., Nuhait, A. O., and Hajj, M. R.: Nonlinear analysis and enhancement of wing-based piezoaeroelastic energy harvesters, *Journal of Sound and Vibration*, 333, 166–177, <https://doi.org/10.1016/j.jsv.2013.08.032>, 2014.
- 815 Bak, C., Zahle, F., Bitsche, R., Kim, T., Yde, A., Henriksen, L. C., Hansen, M. H., and Natarajan, A.: Description of the DTU 10 MW reference wind turbine, DTU Wind Energy Report-I-0092, DTU Vindenergi, 2013.
- Ball, A. A.: CONSURF. Part 1: Introduction of the conic lofting tile, *Computer-aided design*, 25, 513–520, [https://doi.org/10.1016/0010-4485\(93\)90082-Y](https://doi.org/10.1016/0010-4485(93)90082-Y), 1993.
- Bedon, G., Castelli, M. R., and Benini, E.: Evaluation of the effect of rotor solidity on the performance of a H-Darrieus turbine adopting a blade element-momentum algorithm, *World Academy of Science, Engineering and Technology*, 6, 916–921, 2012.
- 820 Beltramo, E., Pérez Segura, M. E., Rocca, B. A., Valdez, M. F., Verstraete, M. L., and Preidikman, S.: Constructive Aerodynamic Interference in a Network of Weakly Coupled Flutter-Based Energy Harvesters, *Aerospace*, 7, 167, <https://doi.org/10.3390/aerospace7120167>, 2020.
- Bhagwat, J. M. and Leishman, J. G.: *Generalized Viscous Vortex Model for Application to Free-Vortex Wake and Aeroacoustic Calculations*, University of Maryland, College Park, 2002.
- Biran, A.: Chapter 6 - Surfaces, in: *Geometry for Naval Architects*, edited by Biran, A., pp. 259–302, Butterworth-Heinemann, <https://doi.org/https://doi.org/10.1016/B978-0-08-100328-2.00016-X>, 2019.
- 825 Bogateanu, R., Frunzulică, F., and Cardos, V.: Unsteady Free-Wake Vortex Particle Model for HAWT, in: *AIP Conference Proceedings*, vol. 1281, pp. 1855–1858, American Institute of Physics, 2010.
- Chen, Y.-C., Fosdick, R., and Fried, E.: Representation of a smooth isometric deformation of a planar material region into a curved surface, *Journal of Elasticity*, 130, 145–195, <https://doi.org/10.1007/s10659-017-9637-2>, 2018.
- 830 Chorin, A. J.: *Vorticity and Turbulence*, Springer-Verlag, New York Inc., 1994.
- Colmenares, J. D., López, O. D., and Preidikman, S.: Computational study of a transverse rotor aircraft in hover using the unsteady vortex lattice method, *Mathematical Problems in Engineering*, 2015, 1–9, <https://doi.org/10.1155/2015/478457>, 2015.
- CSSC Haizhuang: CSSC Haizhuang H260-18MW offshore wind turbine, <http://cssc-hz.com/?en/enNews/NewsReleases/148.html>, 2023.
- Fernandez-Guasti, M.: Analytic geometry of some rectilinear figures, *International Journal of Mathematical Education in Science and Technology*, 23, 895–913, <https://doi.org/10.1080/0020739920230607>, 1992.
- 835 Fong, C.: Homeomorphisms between the circular disc and the Square, *Handbook of the Mathematics of the Arts and Sciences*, pp. 123–148, 2021.
- Gaertner, E., Rinker, J., Sethuraman, L., Zahle, F., Anderson, B., Barter, G. E., Abbas, N. J., Meng, F., Bortolotti, P., Skrzypinski, W., et al.: IEA wind TCP task 37: definition of the IEA 15-megawatt offshore reference wind turbine, Technical Report NREL/TP-5000-75698, National Renewable Energy Lab.(NREL), Golden, CO (United States), 2020.
- 840 Garrel, A. V.: *Development of a wind turbine aerodynamics simulation module*, 2003.
- Gebhardt, C. G.: *Desarrollo de simulaciones numéricas del comportamiento aeroelástico de grandes turbinas eólicas de eje horizontal*, Phd. dissertation, Facultad de Ciencias Exactas, Físicas y Naturales, Universidad Nacional de Córdoba, Argentina, 2012.
- Gebhardt, C. G. and Rocca, B. A.: Non-linear aeroelasticity: an approach to compute the response of three-blade large-scale horizontal-axis wind turbines, *Renewable Energy*, 66, 495–514, 2014.
- 845 Gebhardt, C. G., Preidikman, S., and Massa, J. C.: Numerical simulations of the aerodynamic behavior of large horizontal-axis wind turbines, *International Journal of Hydrogen Energy*, 35, 6005–6011, 2010.



- Griffith, D. T. and Ashwill, T. D.: The Sandia 100-meter all-glass baseline wind turbine blade: SNL100-00, Sandia Report SAND2011-3779, Sandia National Laboratories, 2011.
- 850 Hannover, L. U.: Collaborative Research Centre 1463: Integrated design and operation methodology for offshore megastructures, <http://website-url.com>, accessed on June 15, 2023, 2021.
- Hansen, M. O. L.: Aerodynamics of wind turbines, Earthscan, London, 2008.
- Hau, E. and von Renouard, H.: Wind turbines: fundamentals, technologies, application, economics, Springer New York, 2003.
- Hazebrouck, G.: OpenVOGEL: Free software tools for aircraft design, <https://github.com/OpenVOGEL>, Accessed June 14, 2023.
- 855 Hente, C., Rocchia, B., Rolfes, R., and Gebhardt, C.: On a linearization strategy for the unsteady vortex-lattice method with applications in nonlinear aerodynamics and aeroelasticity, To be submitted to AIAA Journal, –, –, 2022.
- Jonkman, J., Butterfield, S., Musial, W., and Scott, G.: Definition of a 5-MW reference wind turbine for offshore system development, Tech. rep., National Renewable Energy Lab.(NREL), Golden, CO (United States), 2009.
- Kandil, O., Mook, D., and Nayfeh, A.: Nonlinear prediction of aerodynamic loads on lifting surfaces, *Journal of Aircraft*, 13, 22–28, 1976.
- 860 Katz, J. and Plotkin, A.: *Low-Speed Aerodynamics*, vol. 13, Cambridge university press, 2001.
- Lambert, T. and Dimitriadis, G.: Induced drag calculations with the unsteady vortex lattice method for cambered wings, *AIAA Journal*, 55, 668–672, 2017.
- Larwood, S., Van Dam, C., and Schow, D.: Design studies of swept wind turbine blades, *Renewable Energy*, 71, 563–571, 2014.
- Lee, H. and Lee, D.-J.: Effects of platform motions on aerodynamic performance and unsteady wake evolution of a floating offshore wind
- 865 turbine, *Renewable Energy*, 143, 9–23, 2019.
- Lee, H., Sengupta, B., Araghizadeh, M. S., and Myong, R. S.: Review of vortex methods for rotor aerodynamics and wake dynamics, *Advances in Aerodynamics*, pp. 1–36, <https://doi.org/10.1186/s42774-022-00111-3>, 2022.
- Liu, Y., Xiao, Q., Incecik, A., Peyrard, C., and Wan, D.: Establishing a fully coupled CFD analysis tool for floating offshore wind turbines, *Renewable Energy*, 112, 280–301, 2017.
- 870 Muñoz-Simón, A., Palacios, R., and Wynn, A.: Some modelling improvements for prediction of wind turbine rotor loads in turbulent wind, *Wind Energy*, 25, 333–353, 2022.
- Nguyen, A. T., Kim, J.-K., Han, J.-S., and Han, J.-H.: Extended unsteady vortex-lattice method for insect flapping wings, *Journal of Aircraft*, 53, 1709–1718, 2016.
- Nigam, P. K., Tenguria, N., and Pradhan, M. K.: Analysis of horizontal axis wind turbine blade using CFD, *International Journal of Engineering, Science and Technology*, 9, 46–60, 2017.
- 875 Perez-Becker, S., Papi, F., Saverin, J., Marten, D., Bianchini, A., and Paschereit, C. O.: Is the Blade Element Momentum theory overestimating wind turbine loads?—An aeroelastic comparison between OpenFAST’s AeroDyn and QBlade’s Lifting-Line Free Vortex Wake method, *Wind Energy Science*, 5, 721–743, 2020.
- Pérez Segura, M. E., Mook, D. T., and Preidikman, S.: General-Purpose Object-Oriented Framework for Vorticity-Dominated Flow Simulation, *Journal of Aerospace Information Systems*, 17, 562–580, 2020.
- 880 Preidikman, S.: Numerical Simulations of Interactions Among Aerodynamics, Phd. dissertation, Department of Engineering Science and Mechanics, Virginia Polytechnic Institute and State University, Blacksburg, VA, 1998.
- Rocchia, B. A.: UVLMeshGen: UVLM-oriented mesh generator for wind turbines, <https://github.com/brunorocchia/UVLMeshGen-mesh-generator>, 2023.



- 885 Roccia, B. A., Preidikman, S., Massa, J. C., and Mook, D. T.: Modified unsteady vortex-lattice method to study flapping wings in hover flight, *AIAA journal*, 51, 2628–2642, <https://doi.org/10.2514/1.J052262>, 2013.
- Roccia, B. A., Verstraete, M. L., Ceballos, L. R., Balachandran, B., and Preidikman, S.: Computational study on aerodynamically coupled piezoelectric harvesters, *Journal of Intelligent Material Systems and Structures*, 31, 1578–1593, <https://doi.org/10.1177/1045389X20930093>, 2020.
- 890 Roccia, B. A., Verstraete, M. L., Dimitriadis, G., Bruels, O., and Preidikman, S.: Unsteady aerodynamics and nonlinear dynamics of free falling rotating seeds, in: *Proceedings of the International Conference on Noise and Vibration Engineering, ISMA 2018, KUL, September 2018*.
- Sant, T. and Cuschieri, K.: Comparing three aerodynamic models for predicting the thrust and power characteristics of a yawed floating wind turbine rotor, *Journal of Solar Energy Engineering*, 138, 2016.
- 895 Schepers, G.: Avatar: Advanced aerodynamic tools of large rotors, in: *33rd Wind Energy Symposium*, p. 0497, 2015.
- Simpson, R., Palacios, R., and Murua, J.: Induced-drag calculations in the unsteady vortex lattice method, *AIAA journal*, 51, 1775–1779, 2013.
- Stanford, B. K. and Beran, P. S.: Analytical Sensitivity Analysis of an Unsteady Vortex-Lattice Method for Flapping-Wing Optimization, *Journal of Aircraft*, 47, 647–662, <https://doi.org/10.2514/1.46259>, 2010.
- 900 Terry, E.: CFD: the truth and the tales, <https://actiflow.com/cfd-the-truth-and-the-tales-2/>, 2018.
- Torabi, F.: *Fundamentals of Wind Farm Aerodynamic Layout Design*, Academic Press, London, 2022.
- Verstraete, M. L., Preidikman, S., Roccia, B. A., and Mook, D. T.: A numerical model to study the nonlinear and unsteady aerodynamics of bioinspired morphing-wing concepts, *International Journal of Micro Air Vehicles*, 7, 327–345, 2015.
- Verstraete, M. L., Roccia, B. A., Mook, D. T., and Preidikman, S.: A co-simulation methodology to simulate the nonlinear aeroelastic behavior of a folding-wing concept in different flight configurations, *Nonlinear Dynamics*, 98, 907–927, <https://doi.org/10.1007/s11071-019-05234-9>, 2019.
- 905 Verstraete, M. L., Ceballos, L. R., Hente, C., Roccia, B. A., and Gebhardt, C. G.: A code-to-code benchmark for simulation tools based on the nonlinear unsteady vortex-lattice method, *Journal of Aerospace Information Systems*, Accepted, –, 2023.
- Vestas: Vestas V236-15.0 MW wind turbine, <https://www.vestas.com/en/products/offshore/V236-15MW>, 2022.
- 910 Wie, S. Y., Lee, S., and Lee, D. J.: Potential panel and time-marching free-wake-coupling analysis for helicopter rotor, *Journal of Aircraft*, 46, 1030–1041, <https://doi.org/10.2514/1.40001>, 2009.
- WinDS: The Wake Induced Dynamic Simulator (WInDS), <https://www.umass.edu/windenergy/research/software>, Accessed June 14, 2023.